Journal of Materials Research and Technology 43 (2026) 3228–3244

Contents lists available at ScienceDirect

Journal of Materials Research and Technology

journal homepage: www.elsevier.com/locate/jmrt

Cellular automata simulations of texture evolution in flat-top laser additively manufactured Hastelloy-X

Fabien Briffod *, Phuangphaga Daram, Tomonori Kitashima, Makoto Watanabe

Research Center for Structural Materials, National Institute for Materials Science, 1-2-1 Sengen, Tsukuba, 305-0047 Ibaraki, Japan

ARTICLE INFO

Keywords:
Cellular automata
Additive manufacturing
Texture
Microstructure

ABSTRACT

The present study investigates the influence of process parameters, nucleation density, and stochastic effects on the microstructure evolution of Hastelloy X samples fabricated by selective laser melting on near single crystal Ni substrates using a flat top laser. Experiments and cellular automata simulations were performed to analyze crystallographic texture and M-index evolution along the build height as a function of laser power, scan speed and heterogeneous nucleation density. The results show that higher laser powers and lower scan speeds promote epitaxial growth, stabilizing the texture, while lower energy densities lead to finer grains and increased high-angle grain boundaries due to enhanced nucleation. A nucleation density of 10–20 × 10^{12} m^{-3} provided the closest agreement in terms of texture strength evolution with most experimental observations while higher nucleation densities lead to a weakening of the texture combined with a faster transition from the initial $\{001\}_z\langle 110\rangle_x$ texture of the substrate to a $\{001\}_z\langle 100\rangle_x$ texture. Additionally, microstructure variability due to stochastic nucleation was found to be process-dependent, with some conditions exhibiting stable, repeatable texture evolution, while other conditions showed high sensitivity to random seed selection. These findings highlight the importance of probabilistic modeling approaches for improving the reliability and robustness of AM microstructure simulations.

1. Introduction

Additive manufacturing (AM) is progressively transforming the field of metallic structural materials by enabling the fabrication of complex three-dimensional components with a high degree of geometric freedom. Unlike traditional subtractive manufacturing techniques, such as cutting and drilling, which involve material removal, AM builds parts layer-by-layer, allowing for more intricate designs and reduced material waste [1–3]. Among the various AM techniques, powder bed fusion with laser beam (PBF-LB) has emerged as one of the most widely applied methods for producing metallic components with high dimensional accuracy. In the PBF-LB process, a focused laser beam locally melts individual powder layers, which then solidify to form fully dense parts with minimal post-processing requirements. This approach not only facilitates the production of complex geometries but also offers advantages in terms of material utilization and customization [4].

The microstructure produced by the AM process differs significantly from that obtained through conventional manufacturing methods such as casting, forging, or rolling. In PBF-LB processes, microstructural features are highly sensitive to various process parameters, including laser power, scan velocity, scanning path strategy, and hatching distance as they directly affect the melt pool morphology and local cooling rate [5–7]. As a result, there is a growing interest in predicting and controlling key microstructural characteristics such as grain morphology and crystallographic texture by adjusting these parameters to enhance mechanical properties [8–11]. This capability is particularly important for applications requiring superior mechanical performance, such as turbine blades, where single-crystal (SX) microstructures are preferred for their improved creep resistance. Several studies have demonstrated that scanning strategies can significantly influence the development of strong crystallographic textures. For instance, a bidirectional scanning strategy without rotation between layers was found to produce a pronounced $\{011\}_z\langle 100\rangle_x$ texture in a body-centered cubic (bcc) Ti-15Mo-5Zr-3Al alloy, with the z-axis aligned with the build direction (BD) and the x-axis aligned with the scan direction [8]. In contrast, the introduction of a 90° rotation between successive layers reoriented the texture towards a $\{001\}_z\langle 100\rangle_x$ configuration. The stability of the obtained crystallographic texture was found to depend on the scan strategy [11]. In addition, varying the laser scan velocity and rotation angle between layers were found to significantly affect the crystallographic texture in a 316L austenitic stainless steel [9,12].

Most PBF-LB studies have employed Gaussian laser beams, and numerous investigations have demonstrated that grain morphology and

---

* Corresponding author.
E-mail address: BRIFFOD.Fabien@nims.go.jp (F. Briffod).

https://doi.org/10.1016/j.jmrt.2026.06.251
Received 21 May 2026; Accepted 25 June 2026
Available online 30 June 2026
2238-7854/© 2026 The Authors. Published by Elsevier B.V. This is an open access article under the CC BY-NC-ND license (http://creativecommons.org/licenses/by-nc-nd/4.0/).

crystallographic texture can be tailored through the optimization of laser power, scan velocity, hatch spacing, and scan strategy [8–11]. However, due to their relatively small spot size and characteristic melt-pool geometry, Gaussian lasers generally produce microstructures containing a significant fraction of high-angle grain boundaries (HAGBs). More recently, flat-top (top-hat) lasers have attracted attention because their nearly uniform power distribution and larger spot diameters promote conduction-mode melting with a shallow and near-planar melt-pool bottom [13,14]. These conditions favor directional epitaxial growth and have been shown to significantly reduce HAGB density, enabling the formation of strongly textured and near SX microstructures [14–16]. Consequently, understanding and controlling texture development under flat-top laser processing has become an important research topic.

Optimizing PBF-LB process parameters through experimental trial-and-error is both time-consuming and costly. Consequently, integrated computational materials engineering (ICME) approaches have emerged as valuable tools for establishing process–structure relationships and accelerating process optimization. Among the available microstructure prediction methods, the cellular automata (CA) approach has become particularly popular because it can efficiently couple thermal fields with grain growth and texture evolution during solidification [17–30]. Most CA studies reported in the literature have focused on conventional Gaussian laser systems, where the thermal fields are obtained either from analytical heat-source models or from numerical heat-transfer simulations calibrated against experimentally measured melt-pool dimensions. These studies have successfully reproduced key microstructural features such as grain morphology, texture development, and grain selection mechanisms over a wide range of materials and processing conditions. Despite this success, CA predictions remain sensitive to numerical parameters, material properties, nucleation assumptions, and stochastic effects [31–33]. Furthermore, most studies validate the model against a limited number of experimental conditions, making it difficult to assess its robustness across a broad process window. This limitation is particularly relevant for flat-top laser systems, whose melt-pool geometries and solidification conditions differ significantly from those typically observed with Gaussian beams. Therefore, systematic validation and uncertainty assessment remain important challenges for the application of CA models to additive manufacturing.

In our recent experimental study [34], we systematically mapped the texture evolution of flat-top laser processed Hastelloy-X over a wide range of laser powers, scan velocities, and substrate preheating conditions. The results revealed pronounced texture transitions, demonstrating that the balance between epitaxial growth and grain nucleation is highly sensitive to the processing conditions. However, the underlying mechanisms governing these transitions could not be fully resolved from experiments alone due to the limited access to transient melt-pool thermal conditions and competitive grain growth dynamics. In parallel, we developed a coupled finite-difference–cellular automata (FDM–CA) framework capable of linking transient thermal fields to solidification microstructure evolution [35]. While the framework successfully reproduced grain morphology and texture development, its validation was limited to a restricted set of processing conditions. Therefore, the objective of the present study is to apply the FDM–CA framework to the broader experimental dataset generated using flat-top laser processing and to assess its ability to reproduce the observed texture transitions. Particular attention is given to the influence of melt-pool geometry, thermal gradients, and nucleation behavior on texture evolution.

2. Materials and methods

2.1. Thermal field modeling

2.1.1. Heat transfer model

The evolution of the three-dimensional transient temperature field in this study was determined by solving the heat equation under appropriate boundary conditions and heat sources. The general form of the heat equation is expressed as:

$$\rho(T)c_p(T)\frac{\partial T}{\partial t} = \nabla \cdot (\lambda(T)\nabla T) + Q \tag{1}$$

where $\rho(T)$, $c_p(T)$, and $\lambda(T)$ denote the temperature-dependent density, heat capacity, and thermal conductivity of the material, respectively. The term Q represents the volumetric rate of internal heat generation, acting as either a source or a sink. To model the flat-top laser, a three-dimensional volumetric heat source model based on a super-Gaussian distribution was applied [36]:

$$Q_{\text{laser}}(x, y, z) = \frac{\eta P}{V_0} \exp\left(- \left[\frac{\Delta x^2}{r_x^2(z)} + \frac{\Delta y^2}{r_y^2(z)} \right]^{k/2} \right) \tag{2}$$

where η is the laser absorption coefficient of the material, P is the laser power, and V_0 is the volume integral of the distribution. The terms Δx and Δy represent the x- and y-components of the relative distance between a material point and the laser beam center, while $r_x(z)$ and $r_y(z)$ denote the distribution radii along the x- and y-directions. The parameter k controls the shape of the distribution. The evolution of the distribution radii along the depth direction (z-direction) is described by:

$$r_i(z) = \frac{2\sigma_i}{\sqrt[k]{2}} \left(1 - \left| \frac{\Delta z}{d} \right|^m \right)^{1/m}, \quad i \in x, y \tag{3}$$

where Δz is the z-component of the relative distance between the material point and the laser center, $2\sigma_i$ represents the half-widths of the distribution, d is the depth of the heat source, and m is the volumetric shape parameter. Finally, the volume integral of the distribution is given by:

$$V_0 = \pi \Gamma \left(1 + \frac{2}{k}\right) \left(\frac{2\sigma_x}{\sqrt[k]{2}}\right) \left(\frac{2\sigma_y}{\sqrt[k]{2}}\right) d \left[\frac{\Gamma\left(1+\frac{1}{m}\right) \Gamma\left(1+\frac{2}{m}\right)}{\Gamma\left(1+\frac{3}{m}\right)} \right]. \tag{4}$$

By adjusting the parameters k and m, the model can reproduce a wide range of heat source distributions. For instance, when $k = m = 2$, the distribution approximates a Gaussian ellipsoid. A comprehensive analysis of the influence of these parameters on the heat source is provided in the original Ref. [36].

The free surface of the material experiences heat loss due to convection and radiation, driven by the thermal difference with the surrounding atmosphere. The heat loss due to convection is given by:

$$Q_c = h(T - T_{\text{amb}}) \tag{5}$$

where h is the heat transfer coefficient (10 W m^{-2} K^{-1}), and T_{amb} is the ambient temperature. The heat loss due to radiation is expressed as:

$$Q_r = \sigma_B \epsilon (T^4 - T_{\text{amb}}^4) \tag{6}$$

where σ_B is the Stefan–Boltzmann constant (5.67×10^{-8} Wm^{-2} K^{-4}), and ϵ is the emissivity of the surface taken as 0.3.

The heat equation was solved on a discretized regular grid ($\Delta x = \Delta y = \Delta z$) using the forward time-centered space (FTCS) finite difference method (FDM). This explicit scheme is computationally efficient but conditionally stable, requiring the time increment Δt to satisfy the following stability condition:

$$\Delta t \leq \frac{\Delta x^2}{6\kappa} \tag{7}$$

where $\kappa = \lambda/(\rho c_p)$ is the thermal diffusivity. Since the material properties vary with temperature, a stable time increment was dynamically computed at each iteration. The FDM model was implemented in Julia, leveraging its multi-threading capabilities for improved computational performance.

Table 1
Linear energy density in J/mm of the different single track experiments.

Laser power	Scanning speed [mm s^{-1}]					
[W]	200	250	300	350	400	500
1000	5	4	3.3	2.8	2.5	2
700	3.5	2.8	2.3	2	1.75	1.4
600	3	2.4	2	1.7	1.5	1.2
500	2.5	2	1.6	1.4	1.25	1
400	2	1.6	1.3	1.14	1	–
300	1.5	1.2	1	–	–	–

2.1.2. Single track experiments

To calibrate the model, a series of single-track experiments were conducted on a HX substrate without powder using a flat top laser of spot size 700 μm in a SLM 280 HL (SLM Solutions, Germany). The experimental results used here were previously reported in our recent publication [34]. The experiments varied laser power, scanning velocity, and substrate temperature. The experimental conditions are summarized in Table 1. Laser power ranged from 300 to 1000 W, while scanning speeds varied between 200 and 500 mm/s, resulting in linear energy densities from 1 to 5 J/mm. For each condition listed in Table 1, five initial substrate temperatures were examined: 298, 373, 473, 573, and 673 K, resulting in a total of 160 unique conditions. Two single-track scans were performed for each condition. The cross-sections of the resulting melt pools were analyzed using optical microscopy following metallographic polishing and chemical etching. The width and depth of each melt pool were measured and used to calibrate the numerical model parameters.

2.1.3. Single track simulations

The heat transfer model was first applied to reproduce the melt pool dimensions of single-track experiments. A computational domain of 4 × 2 × 2 mm in the x-, y-, and z-directions, respectively, was considered, with a uniform mesh size of 20 μm. Throughout the present manuscript the (x–y) plane corresponds to the plane scanned by the laser while the z-direction corresponds to the build direction (BD). The laser traveled along the x-direction, starting from one edge of the domain, centered along the y-axis, and positioned at the top of the z-direction. The free surface irradiated by the laser was also subjected to radiative and convective loss while all the remaining faces were given zero-flux Neumann boundary conditions (adiabatic). All experimental conditions outlined in the previous section were simulated numerically.

Temperature-dependent material properties, including density, heat capacity, and thermal conductivity of the H-X alloy, were obtained from literature [37] and are illustrated in Fig. 1. The alloy has a solidus temperature of 1533 K and a liquidus temperature of 1628 K. The density decreases with temperature, while heat capacity and thermal conductivity increase. A sharp change in all three properties is observed at the solid–liquid transition.

The remaining parameters to be calibrated from the experimental data were the laser absorptivity η, the half-width of the distribution σ_i assumed to be the same in the x- and y-direction, the depth of the heat source d and the laser shape parameters k and m. To this end, the envelope of the melt pools were extracted and compared with the experimental ones.

2.2. Microstructure modeling

2.2.1. Cellular automata principle

The simulation of the three-dimensional solidified microstructure formed during AM processes is based on the CA method. In this study, the open-source software ExaCA [28] was used. The basic principles of the method are summarized below, while a more detailed description can be found in the original reference.

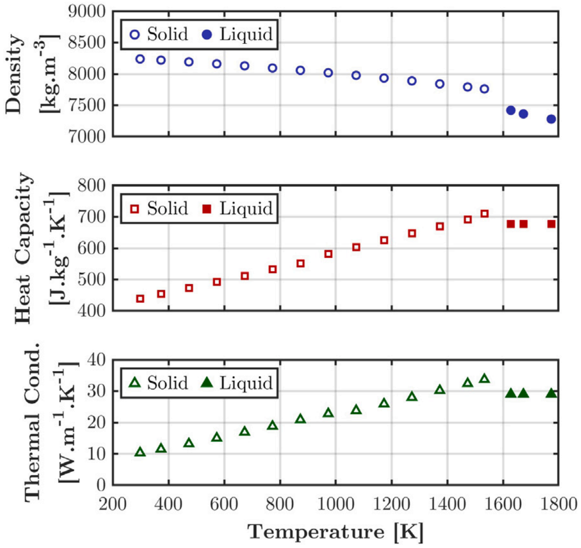

Fig. 1. Thermophysical properties of Hastelloy-X taken from literature [37].

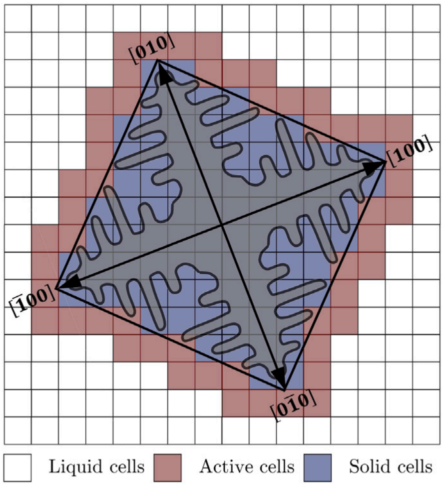

Fig. 2. Two-dimensional schematic of the envelop approximation for the dendrite morphology with the definition of the liquid, active and solid cells.

In the CA model, the detailed dendrite morphology and the preferential growth along the ⟨100⟩ directions in cubic crystals are not physically resolved. Instead, they are phenomenologically approximated by representing the grain envelope as a regular octahedron. This octahedron surrounds both the solid dendrite and the interdendritic liquid region, with its vertices aligning with the ⟨100⟩ tips of the dendrite. Within this approximation, each cell in the model exists in one of three states: liquid, solid, or active as depicted in the schematic diagram in Fig. 2. The active state represents the phase front, separating the liquid and solid regions. A cell transitions to solid once its center is fully enclosed by the octahedral envelope. At this point, a new octahedral envelope is assigned to the captured cell, following the decentered octahedron growth algorithm [38], which reduces grid-induced growth bias favoring specific grain orientations.

The growth velocity of the envelope's vertices along their respective ⟨100⟩ directions is approximated using an interfacial response function, which depends on the local undercooling temperature, ΔT. This function takes the form of a third-order polynomial derived from the Kurz–Giovanola–Trivedi (KGT) model [39]:

$$v(\Delta T) = A\Delta T^3 + B\Delta T^2 + C\Delta T + D \tag{8}$$

where A, B, C and D are fitting parameters.

Heterogeneous grain nucleation is incorporated using a stochastic approach. An initial nucleation density, N_0, is used to randomly select a fraction of cells undergoing solidification as potential nucleation sites. Each selected cell is assigned a nucleation undercooling temperature sampled from a Gaussian distribution, $\mathcal{N}(\Delta T_N, \Delta T_\sigma)$, with a mean ΔT_N and standard deviation ΔT_σ. Nucleation occurs if the cell reaches its assigned nucleation undercooling before being captured by a neighboring grain envelope. In this case, the cell is assigned a random crystal orientation and grows as a new grain.

The CA model is coupled with thermal simulations to extract the necessary solidification conditions. The coordinates, melting and solidification times, and cooling rates at solidification are computed for all elements exceeding the melting temperature. These data are then used to calculate the local undercooling temperature during the CA simulation, enabling the simulation of grain growth and nucleation.

2.2.2. Experimental data

The fabrication procedure and the associated EBSD dataset used in this study were previously reported in [34] and are briefly summarized here for completeness. The AM HX samples were fabricated using the same apparatus as in the single-track experiments under an Ar atmosphere. To investigate the effect of the AM process condition on the microstructure, the same conditions as in the single track experiments, reported in Table 1 were applied. The hatching distance was 100 μm, the layer thickness was 30 μm and a zig-zag scanning strategy with a 90° rotation between layers was applied. To minimize the influence of the substrate on microstructure development, the samples were built above an homogeneous near-$\{001\}\langle 100\rangle$ SX-like substrate fabricated using high-purity Ni powder under the conditions described in previous studies [15,16]. The same flat-top laser as in the single-track experiments was used, with a power of 500 W, a scanning speed of 140 mm/s, a hatching distance of 100 μm, a layer thickness of 30 μm, and a zig-zag scanning strategy with a 90° rotation between layers. These conditions were used to build 6 mm-high Ni SX substrates with a diameter of 12 mm. HX samples were then built on top of the Ni SX substrates. A preheat temperature of 200 °C was used to improve the bonding between the Ni substrate and the HX sample.

Following the fabrication, the samples were removed from the holder and polished up to colloidal silica suspension. The microstructures were analyzed by electron backscattered diffraction (EBSD) within a scanning electron microscope (JEOL JSM 7200F) with an acceleration voltage of 20 kV. EBSD characterization was performed using a step size of 1 μm. Pixels with a confidence index below 0.2 were considered unindexed and were reassigned using nearest-neighbor orientation interpolation. After cleanup, pixels with a confidence index greater than 0.2 represented approximately 94%–96% of the measured dataset, depending on the sample. Grain reconstruction was carried out using a minimum misorientation threshold of 5°. HAGBs were defined as boundaries exhibiting a misorientation angle greater than 15°. No minimum grain-size threshold was applied during the reconstruction process. Identical acquisition and post-processing parameters were used for all EBSD datasets analyzed in this work. The EBSD data were analyzed using the open-source texture software MTEX for Matlab [40].

2.2.3. Microstructural and texture descriptors

To quantitatively assess the texture strength evolution along the build direction for different samples, the texture index known as the M-index was calculated [41]. The M-index is defined as:

$$M = \frac{1}{2}\int |f^{\mathrm{U}}_{\mathrm{MDF}}(\theta) - f_{\mathrm{MDF}}(\theta)| d\theta \tag{9}$$

where $f^{\mathrm{U}}_{\mathrm{MDF}}$ and f_{MDF} represent the uncorrelated misorientation distribution function (MDF) of a random uniform distribution and the experimentally obtained MDF from EBSD data, respectively. The M-index ranges from 0 for a completely random texture to 1 for a perfect single crystal. Compared to other texture quantification parameters, such as the peak value of the orientation distribution function (ODF), the J-index or the degree of crystal orientation for a particular $\langle uvw\rangle$ direction relative to a reference direction [42], the M-index offers a more objective measurement. The peak value of the ODF and the J-index are highly sensitive to computational parameters, including the number of data points, the Gaussian half-width angle, and the number of spherical harmonic expansion terms used for ODF calculation [41]. In contrast, the M-index provides a more robust and reliable characterization of texture strength. In addition, the M-index does not require the decision *a priori* of a specific crystal direction relative to a reference direction. For this analysis, the M-index was calculated along the build direction using EBSD data from domains of size 1500 × 50 μm. This domain size was chosen to ensure statistical reliability while capturing the spatial sensitivity across the sample. The resulting M-index values were used to track texture variation and quantify the loss of the initial near-SX texture.

To complement the M-index analysis, several additional descriptors were used to quantitatively compare the experimental and simulated microstructures. The mean grain width was calculated from the horizontal extent of individual grains and used to characterize the degree of columnar grain growth. The density of HAGBs was calculated as the total length of grain boundaries with a misorientation angle greater than 15° divided by the analyzed area. Compared to the HAGB fraction, the HAGB density provides a less threshold-sensitive measure of grain boundary content and enables direct comparison between microstructures exhibiting different grain sizes.

To quantify the evolution of the dominant texture components, the ODF-derived fractions associated with the $\{001\}_z\langle 100\rangle_x$ and $\{001\}_z\langle 110\rangle_x$ texture components, denoted as $f_{\langle 100\rangle}$ and $f_{\langle 110\rangle}$, respectively, were calculated. Orientations located within 20° of the ideal texture component were considered to belong to the corresponding fiber. In addition, the ratio

$$R_{100} = \frac{f_{\langle 100\rangle}}{f_{\langle 100\rangle} + f_{\langle 110\rangle}} \tag{10}$$

was calculated to quantify the relative predominance of the $\{001\}_z\langle 100\rangle_x$ texture component over the $\{001\}_z\langle 110\rangle_x$ component. Finally, the maximum ODF intensity was used as a complementary measure of texture strength and sharpness.

2.2.4. Cellular automata simulations

The ExaCA software was employed to simulate microstructure development during PBF-LB under the same processing conditions as described in the single-track experiments. The simulations were performed on a computational domain of 1.5 × 1.5 × 4.5 mm, consisting of 150 layers with a cell size of 5 μm. This cell size was selected based on a preliminary mesh size analysis (detailed in the next section) to balance computational cost and accuracy while capturing the coarse grain structure of the experimental substrate.

To ensure meaningful comparison with experimental results, a simulated substrate was generated to replicate the near-SX microstructure used in the experiments. Fig. 3(a) presents EBSD maps with inverse pole figure (IPF) color coding along the x- and z-directions (building direction), alongside the ODF plotted on standard triangles and the grain width distribution of the near-SX Ni substrate. The experimental substrate consisted of columnar grains with a mean width of approximately 200 μm and exhibited a strong crystallographic texture, characterized by the [001] direction aligned with the z-axis and the [011] directions aligned with the x- and y-axes. To reproduce this substrate microstructure in the simulation, a CA directional solidification model was performed in ExaCA. Grain orientations for the initial substrate were sampled from the experimentally measured ODF. A thermal gradient of 5.0×10^5 K/m in the z-direction and a uniform cooling rate of 3.0×10^5 K/s were applied. The directional solidification simulation was performed until the simulated grain width distribution closely

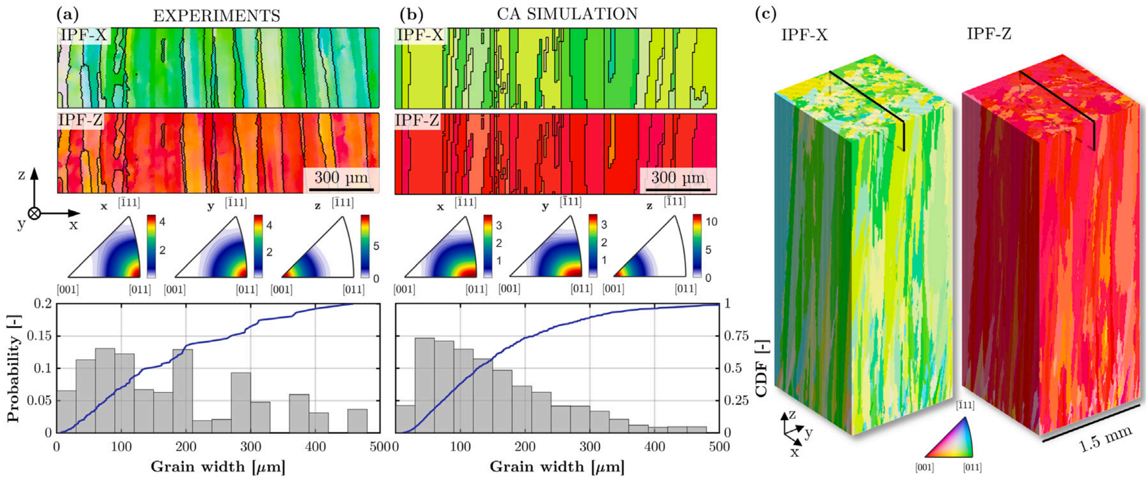

Fig. 3. Comparison between (a) the Ni near-SX microstructure used as a substrate and (b) the microstructure obtained from directional solidification cellular automaton simulations. The inverse pole figure (IPF) maps in the x- and *z*-directions, ODFs on standard triangles, and grain width distributions are shown. (c) The 3D DS microstructure simulated by CA.

matched the experimental data, as shown in Fig. 3. The simulated microstructure at a height of 4 mm was found to reproduce the experimental substrate microstructure with high fidelity in terms of both crystallographic texture and grain width distribution (Fig. 3(b)). In particular, the ODFs plotted on the standard triangles reveal a close agreement between the experimental and simulated substrates, with similar peak locations and intensities. Both microstructures exhibit a strong [001] fiber texture parallel to the build direction and a preferential [011] alignment along the transverse directions. Furthermore, the grain width distributions are in excellent agreement, with both datasets exhibiting a mean grain width of approximately 200 μm and a comparable distribution spread. These results demonstrate that the simulation successfully reproduces not only the characteristic columnar grain morphology of the near-SX substrate, but also its orientation distribution and texture intensity. Consequently, the simulated substrate provides a representative and quantitatively validated initial condition for the subsequent CA simulations of microstructure evolution during additive manufacturing.

The simulation procedure for a single layer is illustrated in Fig. 4. Initially, a layer of powder is added to the top surface of the existing microstructure (Fig. 4(a)). Given the 5 μm cell size and a 30 μm layer thickness, the powder layer consists of six cells in the *z*-direction. The same bidirectional scanning strategy with a 90° rotation per layer was applied to ensure consistency with the previously described process conditions. The thermal field history extracted from single-track simulations was used in the hatching direction, repeating with the bidirectional pattern across the domain. To maintain stable melting and solidification, the thermal history was extracted only within the central region of the domain (between 1 and 2.5 mm in the *x*-direction) to avoid boundary effects that could distort thermal gradients and influence the resulting microstructure.

The number of times a cell melts and solidifies depends on the scanning strategy and process conditions. In the present example, some cells melted up to eight times. To ensure that boundary cells experienced the same number of melt-solidification cycles as those in the interior, the laser scan was extended beyond the computational domain boundaries. This approach ensured that the melt pool width for the first and last track matched the hatching distance, as illustrated in Fig. 4(b–c). This scanning strategy guarantees that the entire computational domain represents a stable process, free from edge effects. In this configuration, more than 20 tracks were required to completely cover the 1.5 × 1.5 mm area (Fig. 4(b)).

The parameters used in the CA simulations are summarized in Table 2. The constants for the interfacial response function defined in Eq. (8) were taken from the literature for HX [43]. To investigate the impact of new grain nucleation on the final microstructure, several nucleation density parameters were tested.

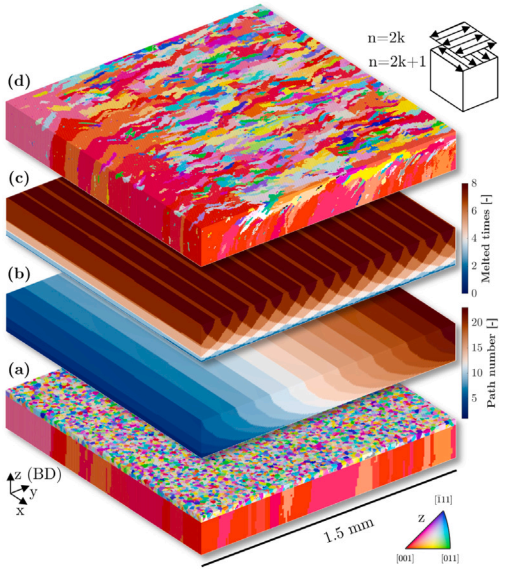

Fig. 4. Procedure for the simulation of one additive manufactured layer by cellular automata. (a) Initial microstructure with a powder layer. (b) Laser scan path number. (c) Number of melted events per cells. (d) Final microstructure.

3. Results

3.1. Melt pool analysis

Fig. 5 presents cross-sectional views of the temperature distribution predicted by the thermal model for a substrate temperature of 473 K and a scanning velocity of 200 mm/s under four different laser powers: 300, 500, 700, and 1000 W. The white contour line represents the current solid–liquid interface, indicating the boundary between the melted and solidified regions. These results were obtained using the following laser parameters: $\eta = 41\%$ (absorption coefficient), $2\sigma_i = 360$ μm (half-width of the laser distribution), $d = 20$ μm (penetration depth), and shape parameters $k = m = 100$. These parameters were

Table 2
AM CA simulation parameters.

Parameter	Symbol	Value	Unit
Cell size	Δx	5	[μm]
Time step	Δt	0.4–1.0	[μs]
Interfacial response fitting parameter 3rd order	A	3.15×10^{-6}	[m s^{-1} K^{-3}]
Interfacial response fitting parameter 2nd order	B	4.6×10^{-10}	[m s^{-1} K^{-2}]
Interfacial response fitting parameter 1st order	C	0.0	[m s^{-1} K^{-1}]
Interfacial response fitting parameter 0th order	D	0.0	[m s^{-1}]
Heterogeneous nucleation density	N_0	10×10^{12}–500×10^{12}	[m^{-3}]
Mean nucleation undercooling	ΔT_N	5	[K]
Standard deviation of nucleation undercooling	ΔT_σ	0.5	[K]
Hatching distance	None	100	[μm]
Offset in build direction for new layers	None	30	[μm]
Number of layers simulated	None	150	[–]

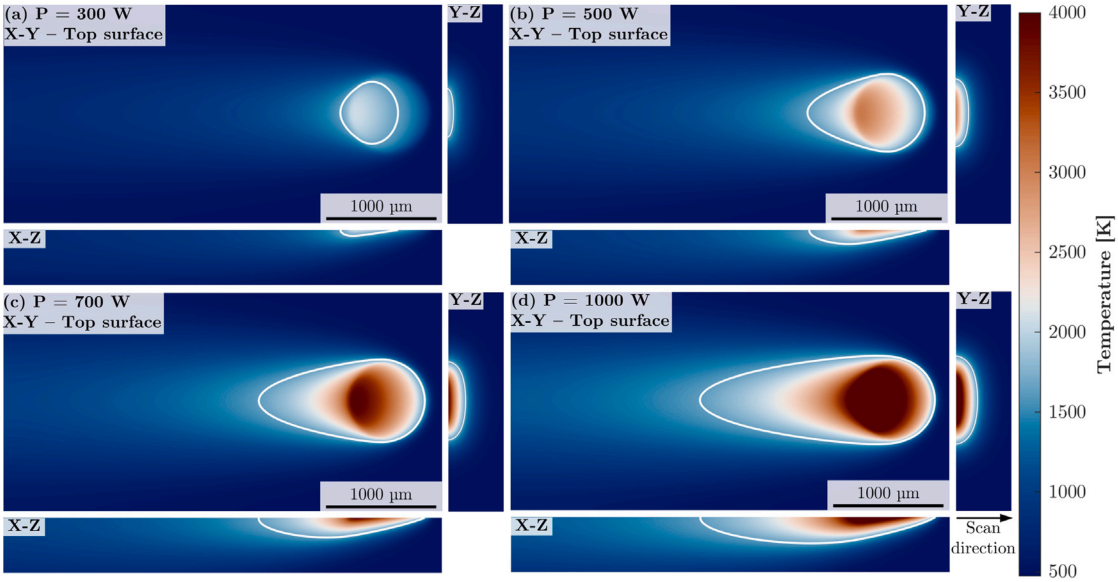

Fig. 5. Examples of temperature distributions predicted by the heat transfer model with a substrate temperature of 473 K, a scan velocity of 200 mm s^{-1} for four different laser power: (a) 300, (b) 500, (c) 700 and (d) 1000 W. The X–Z cross sections were taken at the centerline of the melt pool. The Y–Z cross sections were extracted at the position where the melt pool was the widest.

selected through a manual calibration procedure in which the influence of the different heat-source parameters on the predicted melt-pool geometry was systematically evaluated and compared with experimental observations. No formal optimization algorithm was employed, and the selected parameter set should therefore be regarded as a physically reasonable solution rather than a unique optimum. The low laser penetration depth suggests that a surface heat source model may be sufficient to accurately simulate the flat-top laser profile. Additionally, the high values of the shape parameters k and m indicate a nearly uniform power distribution across the circular laser spot, consistent with the flat-top laser beam configuration. Although the nominal spot diameter was reported as 700 μm, using a distribution half-width of $2\sigma_i = 350$ μm failed to reproduce the experimentally observed melt pool dimensions. Adjusting the half-width to $2\sigma_i = 360$ μm yielded better agreement with experimental measurements for both melt pool width and depth. With the current parameters, the heat flux inside the flat-top laser profile remains uniform. This uniform temperature distribution leads to significant heat accumulation near the rear side of the irradiated domain, as this region experiences the longest irradiation duration. Consequently, the melt pool width, depth, and length increase with laser power due to the higher temperatures generated at higher power levels.

Fig. 6(a) presents examples of experimental melt pool cross-sections at different laser powers and substrate temperatures. The predicted melt pools are superimposed, with the liquidus boundaries highlighted by continuous white lines. Fig. 6(b) shows a quantitative comparison between experimental and numerical melt pool widths and depths for all conditions listed in Table 1 across the range of substrate temperatures. Overall, the selected heat-source parameters reproduce the melt-pool geometry with good agreement, yielding root-mean-square errors (RMSE) of 36.3 μm and 14.8 μm for the melt-pool width and depth, respectively. Although larger discrepancies are observed at the lowest and highest energy densities, i.e., at approximately 1 and 5 J mm^{-3}, the model captures the overall trends in melt-pool dimensions across the investigated process window. The depth-to-width ratio for all experiments remained below 1/3, suggesting that the flat-top laser primarily induced conduction-mode melting without keyhole formation.

3.2. *Experimental microstructure analysis*

The EBSD maps in the xz-plane of HX multilayer microstructures built on top of the Ni near-SX substrates, using the conditions listed in Table 1 and a substrate temperature of 473 K, are shown in Fig. 7. The IPF map is color-coded along the z-direction (BD), and the boundary between the Ni substrate and the HX sample is highlighted. Three (100) pole figures taken at different positions: substrate, 1.5 mm from substrate and 4.5 mm from substrate are also reported next to each EBSD map. It is worth mentioning that the pole figures are plotted in the xy-plane. Some conditions with linear energy densities below 1.2 J/mm failed to produce samples and are not included in the analysis. For most successful builds, a clear microstructural transition

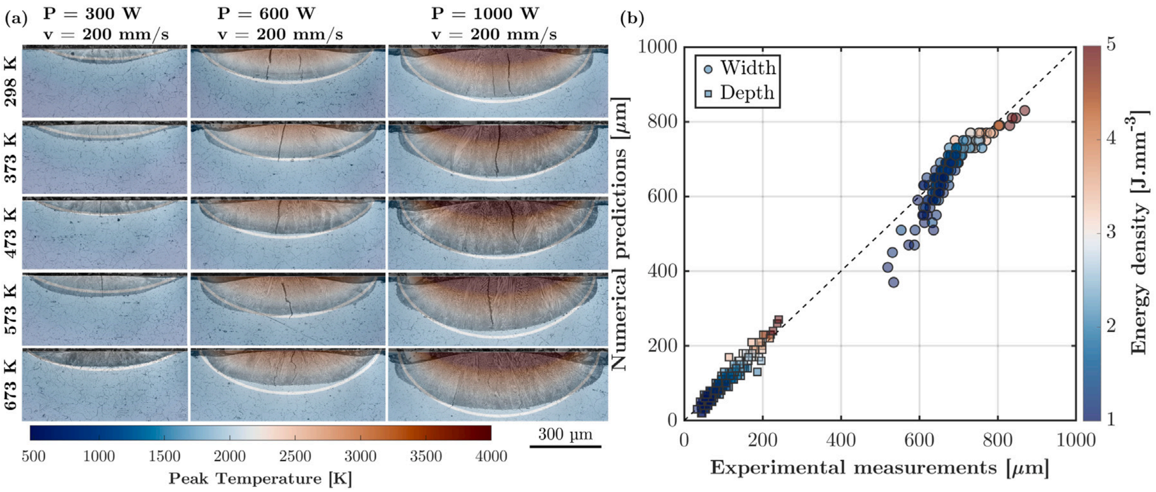

Fig. 6. (a) Experimental melt pool cross sections for different substrate temperature and laser power with superimposed simulated melt pool. White contour lines represent the liquidus boundary. (b) Comparison between the measured and predicted melt pool width and depth for all the conditions reported in Table 1 and all the substrate temperatures.

between the substrate and the HX layers near the interface was not observed. Instead, initial grains from the substrate progressively grew along the build direction. This suggests that the early stages of the build process were dominated by epitaxial growth from the Ni near-SX substrate. However, the initial epitaxial texture was not always preserved throughout the entire HX sample depending on the build condition. The crystallographic texture progressively deviated from the $\{001\}_z\langle110\rangle_x$ orientation characteristic of the Ni substrate. This deviation is attributed to the nucleation of new grains with different orientations as the build progressed. The newly nucleated grains were highly elongated along the build direction and showed a tendency to grow larger at higher laser power and lower scan speeds, corresponding to higher linear energy densities. The increase in grain size with higher linear energy density is consistent with enhanced thermal gradients and slower cooling rates, which favor grain coarsening and reduce the frequency of nucleation events. This effect is particularly evident in regions farther from the interface, where the influence of the substrate diminishes, and grain competition leads to the growth of favorably oriented grains.

Fig. 8 shows the evolution of the M-index along the build height for different process conditions. The near-SX substrate region is highlighted for reference. For all substrates, except the sample built with P = 500 W and v = 200 mm/s, the M-index values remained consistently around 0.6–0.7 in the substrate region. This consistency confirms the reliability of the processing conditions previously identified for manufacturing Ni near-SX samples [15,16]. For each sample, an abrupt drop in the M-index is observed within the first 1–2 mm of build height, indicating a rapid loss of the initial crystallographic texture. The rate and intensity of this drop are not uniform across the different process conditions. Slower and less pronounced decreases in the M-index are associated with higher laser power and higher scan speed. Depending on the process conditions, the M-index behavior after the initial drop varies. For some samples (e.g., P = 500 W, v = 300 mm/s), the M-index continues to decrease throughout the build height, indicating continuous texture degradation. For others (e.g., P = 600 W, v = 250 mm/s), the M-index stabilizes after the initial drop, suggesting a balance between grain growth and nucleation. In the case of high power and low scan speed (e.g., P = 1000 W, v = 200 mm/s), the M-index increases again at later stages, likely due to grain coarsening and the dominance of favorably oriented grains. Final M-index values for all samples were below those of the initial substrate, ranging between 0.1 and 0.5. As a general trend, higher final M-index values were observed for samples built at higher laser power, indicating better texture preservation and reduced random grain nucleation.

Table 3 summarizes the additional microstructural and texture descriptors calculated from the uppermost 200 μm of the EBSD maps shown in Fig. 7. Corresponding values for the near-SX substrate are also included for reference. Overall, the HAGB density decreases with increasing laser power and decreasing scan speed, whereas the mean grain width remains relatively constant across the investigated process window. The texture descriptors reveal a gradual transition from the initial $\{001\}_z\langle110\rangle_x$ texture of the near-SX substrate toward a stronger $\{001\}_z\langle100\rangle_x$ component. This evolution is reflected by the decrease in $f_{\langle110\rangle}$, the corresponding increase in $f_{\langle100\rangle}$, and the resulting increase in the ratio R_{100}. The transition is most pronounced at low laser powers and high scan speeds, whereas the $\{001\}_z\langle110\rangle_x$ component remains dominant for all investigated scan speeds at a laser power of 1000 W. Consistent with these observations, the maximum ODF intensity generally increases with laser power, indicating the development of stronger and sharper crystallographic textures.

3.3. Sensitivity analysis of cell size and time step

Prior to the CA simulations of AM process, a sensitivity analysis was conducted to determine appropriate values for the cell size (Δx) and time step (Δt). The objective was to ensure a balance between computational efficiency and reliable convergence of the predicted microstructure. To achieve this, single-track solidification simulations were performed using the same initial substrate while varying Δx between 2.5, 5.0, and 10.0 μ m, and Δt between 0.1, 1.0, and 10.0 μs. The thermal field for a laser power of 1000 W and a scan velocity of 250 mm/s was applied, and no nucleation events were considered in this analysis. Fig. 9(a) presents the predicted microstructures at the top surface for the nine different parameter combinations, where individual grains are color-coded based on their grain identification (ID) number. To quantitatively assess the effect of mesh resolution, the volume of each grain within the melt pool was calculated and compared with the reference case (Δx = 2.5 μm, Δt = 0.1 μs), which was assumed to provide the most accurate resolution. The relative deviations in grain volume for each condition are shown in Fig. 9(b), and the RMSE was computed for each case to quantify the differences. The results indicate that increasing the cell size has a greater impact on prediction accuracy than increasing the time step. The highest errors were associated with small grains, as a coarser mesh may not fully resolve their structure, leading to significant variations in the number of cells per grain and, consequently, in grain volume estimations. Based on these findings, a cell size of 5.0 μm was chosen for the present study to balance accuracy

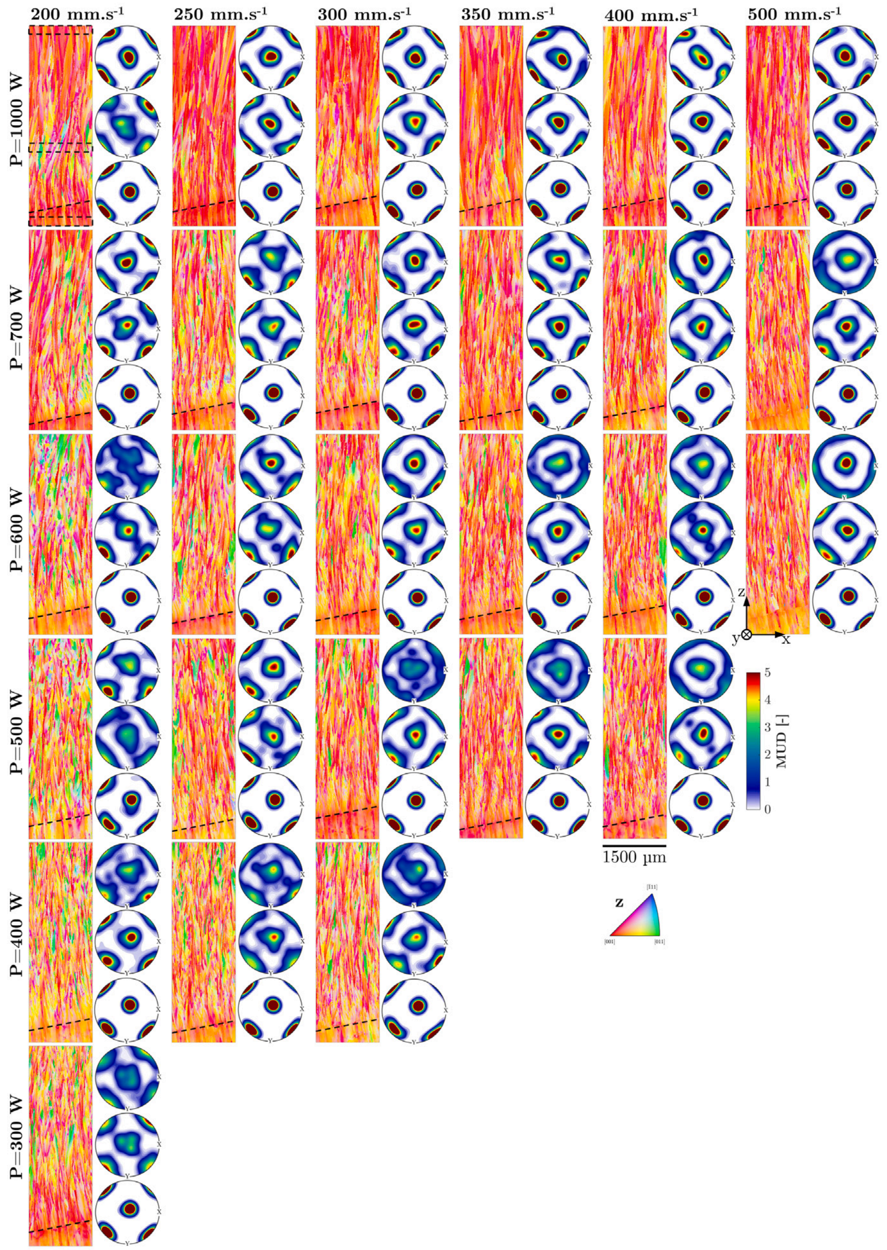

Fig. 7. Experimental EBSD maps in the XZ plane with IPF color coding along the z-direction and corresponding (100) pole figures in the XY plane at three different build height for the different build conditions. Locations of the interface between the near-SX Ni substrate and the built materials are highlighted.

and computational cost. In contrast, variations in Δt showed a minimal effect on RMSE, except for the largest time step ($\Delta t = 10.0$ µs) in cases where $\Delta x = 2.5$ and 5.0 µ m. Interestingly, this effect was not observed for $\Delta x = 10.0$ µm, suggesting that Δx and Δt cannot be optimized independently. To address this, an empirical relationship is often used to determine a suitable time step [30,31]:

$$N = \frac{\Delta x}{v \Delta t} \tag{11}$$

where v is the laser scan speed, and N represents the ratio between the cell size and the liquidus isotherm movement, approximated by the scan speed. Previous studies recommend a threshold of $N \geq 25$ to minimize the influence of the time step on grain growth predictions [30,31]. Applying this criterion to the present case ($\Delta x = 5.0$ µm) yields a time step of $\Delta t = 0.8$ µs, which is consistent with the observation that RMSE values remained low for $\Delta t = 0.1$ and 1.0 µs. Since the scan velocity varied between 200 and 500 mm/s across different simulations, the time step was adjusted accordingly for each condition based on Eq. (11) with $N = 25$. This ensured that temporal resolution remained sufficient to capture grain growth dynamics accurately while maintaining computational efficiency.

3.4. Numerical microstructure analysis

CA simulations of AM were performed under the same conditions as the experiments, using the initial substrate reported in Fig. 3 and the temperature field extracted from single-track simulations with a substrate temperature of 473 K. To investigate the influence of nucleation density on the predicted microstructure, five different nucleation densities (N_0) were examined: 10, 20, 50, 100, and 500 × 10^{12} m^{-3}. Fig. 10 presents the microstructures predicted with a nucleation density of $N_0 = 10 \times 10^{12}$ m^{-3}. The IPF color coding represents crystallographic orientations along the z-direction (BD). Additionally, corresponding (100) pole figures are shown at build heights of 1.5 mm and 4.5 mm. Similar results for other nucleation densities can be found

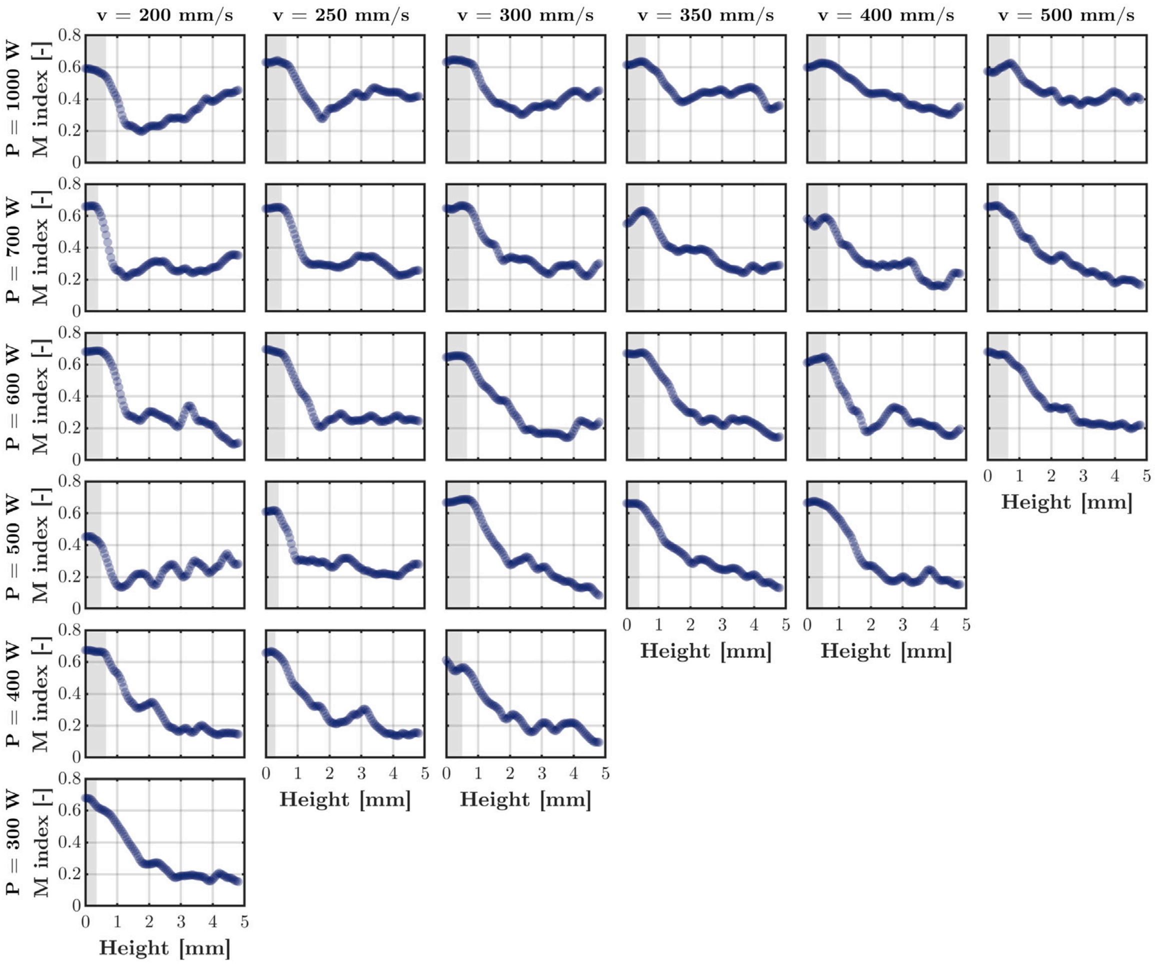

Fig. 8. Variation of the M-index along the build height for the different build conditions.

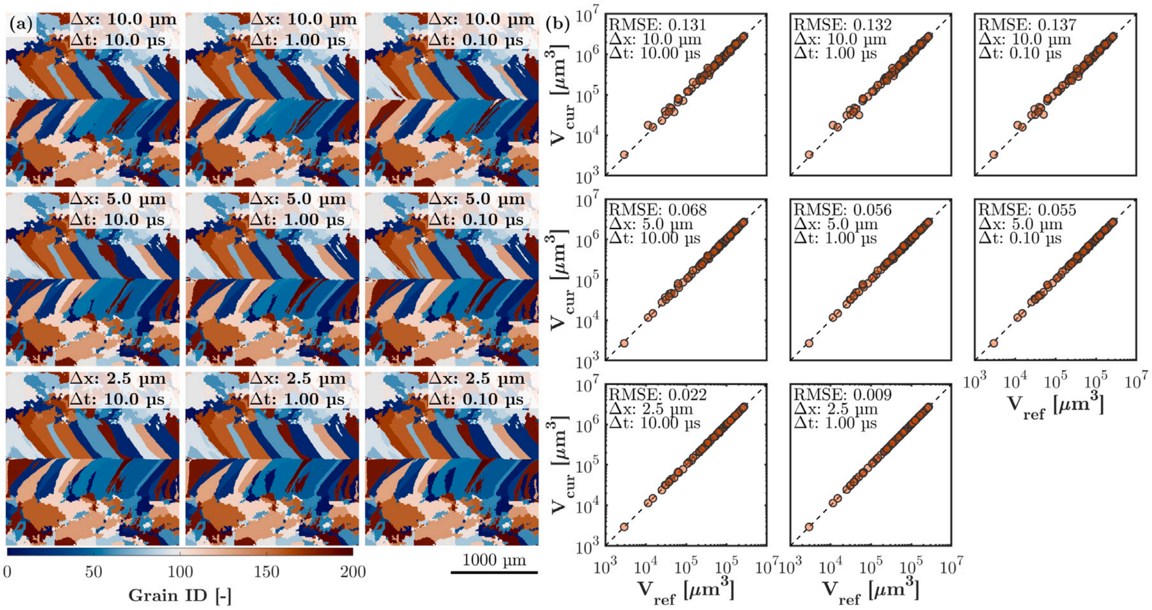

Fig. 9. (a) Top surface cross sections of the single track cellular automata simulations for the different cell size and time step. (b) Comparison of grains volume predicted with the different conditions.

Table 3

Comparison of experimental and simulated ($N_0 = 10 \times 10^{12}$ m^{-3}) microstructural and texture characteristics.

P	v	HAGB density		Mean width		$f_{\langle 100 \rangle}$		$f_{\langle 110 \rangle}$		R_{100}		Max ODF	
[W]	[mm/s]	Exp. [μm^{-1}]	Sim. [μm^{-1}]	Exp. [μm]	Sim. [μm]	Exp. [%]	Sim. [%]	Exp. [%]	Sim. [%]	Exp. [%]	Sim. [%]	Exp. [m.r.d.]	Sim. [m.r.d.]
Substrate		0.003	0.007	176	156	0.6	2.1	52.7	63.0	1.12	3.2	45.0	44.5
300	200	0.063	0.048	43	305	3.7	17.8	19.6	1.9	16	90.6	7.3	12.8
400	200	0.048	0.039	46	297	3.3	26.6	23.3	5	12.4	84.3	10.1	17
400	250	0.052	0.028	44	553	5.8	61.7	21.1	8.1	21.5	88.4	10.9	45.8
400	300	0.052	0.042	48	330	7.8	6.4	14.2	7.7	35.5	45.2	6.1	21
500	200	0.036	0.022	64	397	0.8	53.2	22.1	10.1	3.7	84	11.8	35.6
500	250	0.037	0.032	59	276	2.3	12.7	33.4	14.9	6.4	45.9	12.9	15.1
500	300	0.04	0.042	58	237	4.1	23.5	19.7	16.1	17.3	59.3	6.3	12.9
500	350	0.049	0.036	51	189	7.3	40	21	36.5	25.9	52.3	7.6	26.4
500	400	0.056	0.043	48	235	12.7	6.9	18.9	39.5	40.1	14.9	7.8	17.8
600	200	0.033	0.037	79	243	2.8	16.4	14.3	22.3	16.5	42.5	7.4	24.5
600	250	0.036	0.034	60	291	3.6	14.3	31.3	19.2	10.3	42.6	12.4	13.7
600	300	0.044	0.01	50	925	7.5	77.3	32.7	3.2	18.6	96.1	13	54.6
600	350	0.048	0.045	53	189	9.5	19.4	18.7	19.1	33.6	50.4	9.3	12.5
600	400	0.057	0.028	44	371	8.4	32.7	21.6	13.4	28	71	8.1	19.5
600	500	0.054	0.039	40	292	24.4	27.7	17.1	19.9	58.8	58.1	8.3	18.8
700	200	0.029	0.031	63	246	2.5	26.7	43.6	32.7	5.4	45	16.8	20.6
700	250	0.036	0.042	65	105	2.2	5.4	25.9	39.2	7.7	12.1	11.6	25.6
700	300	0.036	0.032	49	479	4.2	23.5	38.3	12.5	9.8	65.2	15.8	23
700	350	0.041	0.041	50	160	1.8	17.9	36	24.3	4.6	42.4	13.3	15.7
700	400	0.037	0.036	54	431	8.9	23.4	30.4	4.6	22.7	83.5	14.6	23.9
700	500	0.049	0.033	51	267	8.7	30.7	20.7	28.5	29.5	51.9	7.1	18.2
1000	200	0.023	0.036	78	169	1.9	15.9	49	36.6	3.8	30.2	23.3	22.8
1000	250	0.024	0.038	74	185	2.5	13.3	47.8	20.8	4.9	39	19.7	11.8
1000	300	0.025	0.037	117	168	1.5	21.3	51.7	34.6	2.8	38.1	19.4	21.8
1000	350	0.022	0.037	98	281	4.8	27	35.6	9.8	12	73.3	22.6	18.1
1000	400	0.024	0.043	85	155	1.3	10.7	39.9	22.1	3.1	32.5	18.4	14
1000	500	0.032	0.025	63	281	2.9	34.2	49.5	19.2	5.5	64.1	22.4	19.1

in the Supplementary Material. Each simulated microstructure consists of approximately 81 × 10^6 cells. Regardless of process conditions, the simulated microstructures progressively deviate from the initial substrate microstructure due to repeated melting, solidification, and nucleation of new grains. This deviation is particularly evident in the changes observed in the pole figures at a height of 1.5 mm. However, despite continuous remelting, the strong $\{001\}_z$ crystallographic texture along the BD generally persists across all conditions, with the exception of the case at P = 300 W and v = 200 mm s^{-1}, where significant texture evolution occurs. In contrast, the initial $\langle 110 \rangle_x$ texture along the x- and *y*-directions does not always remain stable throughout the build. In several cases, it gradually transitions toward a $\langle 100 \rangle_x$ texture, particularly at low linear energy densities (e.g., P = 400 W, v = 250 mm s^{-1}). This transition suggests that lower energy densities promote grain reorientation, likely due to an increased contribution of nucleation events during solidification.

The additional microstructural and texture descriptors obtained from the simulated microstructures for a nucleation density of $N_0 = 10 \times 10^{12}$ m^{-3} are also reported in Table 3. Corresponding results for the other investigated nucleation densities are provided in the Supplementary Material. The simulated microstructures exhibit a slight reduction in HAGB density with increasing laser power. In contrast, the mean grain width is generally larger than in the experiments and decreases with increasing nucleation density. In several cases, the simulated grain widths exceed the experimental values by a factor of three to ten, indicating that grain coarsening is overestimated in the present framework for low nucleation density. In some cases, such as P = 600 W and v = 300 mm s^{-1}, abnormal grain growth is observed, resulting in exceptionally large grains and a strong reduction in grain boundary density. The texture descriptors indicate a more pronounced evolution of crystallographic texture than observed experimentally. In particular, the decrease in $f_{\langle 110 \rangle}$ and corresponding increase in $f_{\langle 100 \rangle}$ occur more rapidly, resulting in larger values of R_{100} for many process conditions. Consequently, the simulated microstructures tend to exhibit a stronger predominance of the $\{001\}_z\langle 100 \rangle_x$ texture component compared to the experiments. Consistent with this behavior, the maximum ODF intensity is generally higher in the simulations, indicating sharper crystallographic textures and a stronger orientation selection during the simulated build process.

To highlight the influence of nucleation density on the final microstructure, Fig. 11 presents a set of microstructures predicted for a laser power of P = 700 W and a scan velocity of v = 250 mm s^{-1} across five different nucleation densities. The results reveal a clear transition in both grain morphology and crystallographic texture as the nucleation density increases. With increasing nucleation density, the microstructure progressively evolves from coarser columnar grains to a finer, more equiaxed grain structure. Simultaneously, the crystallographic texture shifts from a $\{001\}_z\langle 110 \rangle_x$ orientation to a $\{001\}_z\langle 100 \rangle_x$ configuration, accompanied by a significant decrease in texture intensity. This reduction in intensity suggests that the fraction of grains with $\{001\}_z$ alignment along the BD decreases as nucleation events become more frequent. Moreover, the transition away from the initial microstructure occurs more rapidly at higher nucleation densities. This acceleration is likely due to the increased competition between newly nucleated grains, which disrupts the preferential growth of pre-existing columnar grains. At lower nucleation densities, epitaxial growth from the underlying grains remains dominant, allowing the original texture to persist over a greater build height. In contrast, at higher nucleation densities, the increased frequency of grain nucleation leads to a faster loss of the initial crystallographic texture, resulting in a more randomized grain structure. Similar observations can be made for other microstructures provided in Supplementary Material.

To quantitatively assess the influence of process conditions and nucleation density on the predicted microstructure, the M-index was calculated slice by slice along the build direction and is presented in Fig. 12. Regardless of the process conditions or nucleation density, the M-index initially exhibits a drop from the initial value for the substrate. The rate of this decline increases with nucleation density, consistent with the qualitative trends observed in Fig. 11. Generally, higher nucleation densities result in a deeper drop in M-index, indicating a stronger deviation from the initial substrate texture. Additionally, a reduction in linear energy density, achieved either by increasing the

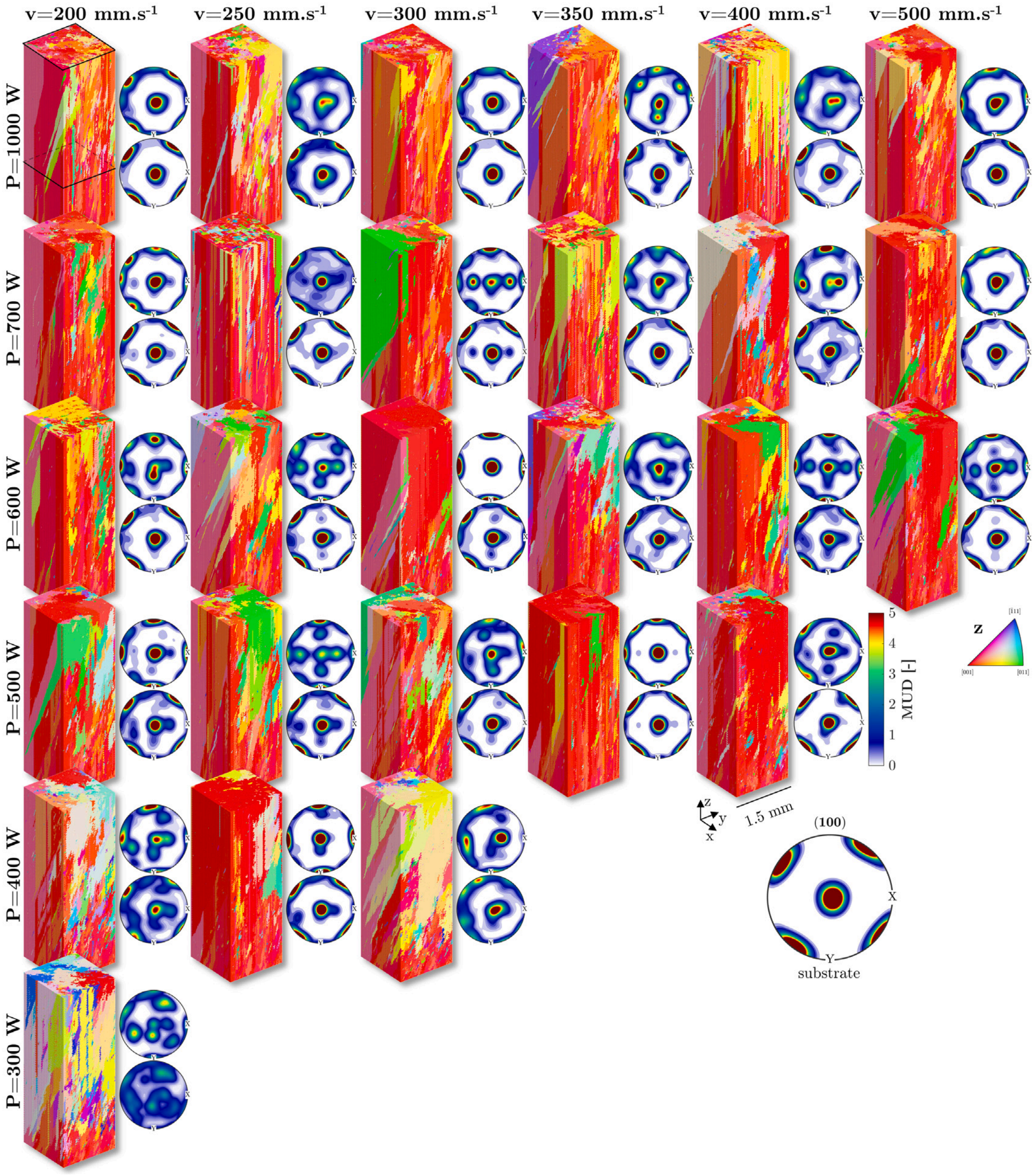

Fig. 10. Numerical microstructures predicted by CA with a nucleation density $N_0 = 10 \times 10^{12}$ m^{-3} and corresponding (100) pole figures in the XY plane at two different build height for the different build conditions. The IPF color coding is along the z-direction.

scan speed or decreasing the laser power, further accelerates the M-index drop for a given nucleation density. Following this initial decline, the M-index exhibits different behaviors, which are consistent with experimental observations. Depending on the process conditions, the M-index may continue to decrease, stabilize, or in some cases, increase before eventually reaching a steady state. A general trend is that stable steady-state microstructures tend to be achieved more rapidly at higher nucleation densities. Conversely, at lower nucleation densities, even after 4.5 mm of build height, the M-index continues to evolve, suggesting that the microstructure remains dynamic and has not yet reached equilibrium. Anomalous increases in the M-index are also observed in certain cases. For instance, at 600 W and 300 mm/s, the M-index rises back to values close to those of the original substrate. This behavior is indicative of abnormal grain growth, where a single grain expands and dominates the majority of the microstructure, as shown in Fig. 10. Such grain coarsening events can significantly alter the final texture and are typically associated with localized reductions in nucleation events, allowing a few grains to grow unchecked. By comparing the evolution of the M-index in the experimental data (Fig. 8) and the simulation results (Fig. 12), a nucleation density of 10 or 20 × 10^{12} m^{-3} appears to provide the best agreement in terms of M-index evolution. This suggests that, within the range of tested conditions, these nucleation densities most accurately replicate the texture development observed in the experiments.

To evaluate the impact of the stochastic nature of nucleation events in the model, two process conditions: P = 700 W, v = 250 mm s^{-1} and P = 600 W, v = 300 mm s^{-1} were simulated while varying the random number generation seed used for the orientation and location of potential nucleation sites. For each condition, nine different seed numbers were used, and a nucleation density of 10 × 10^{12} m^{-3} was applied in both cases. Fig. 13 presents the resulting three-dimensional microstructures, corresponding (100) pole figures at the top of the build, and the evolution of the M-index along the build height for the two process conditions across the nine different seed numbers. In addition, the mean M-index and corresponding

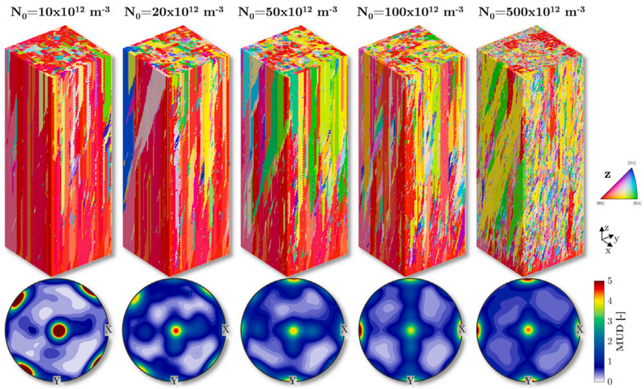

Fig. 11. Numerical microstructures predicted by CA with a laser power P = 700 W, a scan speed v = 250 mm s^{-1} and five different nucleation densities. The corresponding (100) pole figures at the top of the microstructures are also reported.

standard deviation calculated from the nine simulations are reported to provide a quantitative measure of the variability associated with stochastic nucleation. The two process conditions were selected to highlight cases where (1) the microstructure remains largely unaffected by changes in the random seed, leading to stable predictions (Fig. 13(a–c)), and (2) the microstructure exhibits significant variability between different seeds, resulting in unpredictable behavior (Fig. 13(d–f)). For the P = 700 W, v = 250 mm s^{-1} condition, all nine simulated microstructures exhibit highly similar grain structures, closely matching in both crystallographic texture and M-index evolution. Consistent with these observations, the standard deviation of the M-index remains low throughout the build, indicating that the effect of stochastic variations in nucleation is limited and that microstructural evolution is relatively stable and predictable. In contrast, for the P = 600 W, v = 300 mm s^{-1} condition, two out of the nine simulations (seed 1 and seed 3 in Fig. 13(f)) exhibit a pronounced increase in the M-index after the initial drop. This increase is caused by the nucleation and rapid growth of a single dominant grain with a near-$\{001\}_z\langle 100\rangle_x$ orientation, which subsequently extends across almost the entire domain. Additionally, the initial M-index decrease exhibits greater variability across different seeds, resulting in larger standard deviations and suggesting that the early-stage nucleation dynamics are more sensitive to random variations under this process condition. It should be noted that the present analysis was limited to two representative process conditions and is intended to illustrate the potential impact of stochastic nucleation rather than provide a comprehensive uncertainty quantification across the entire process window. Nevertheless, the results demonstrate that microstructure prediction can be either largely insensitive or highly sensitive to random nucleation events depending on the processing conditions.

Finally, an additional series of simulations was performed to investigate the influence of substrate temperature, considering values of 473, 673, 873, and 1073 K and a build condition P = 700 W, v = 250 mm s^{-1}. The results are reported in Fig. 14. The results indicate that increasing the substrate temperature significantly affects the evolution of the crystallographic texture. In particular, a more pronounced initial drop in the M-index is observed at higher substrate temperatures, suggesting an enhanced disruption of the inherited substrate texture during the early stages of the build. However, this effect is followed by a stronger recovery and subsequent increase in the M-index at larger build heights. This behavior indicates that, although elevated substrate temperatures initially promote conditions favorable to nucleation and texture degradation, they ultimately enhance epitaxial growth during later stages of the build.

4. Discussions

4.1. *Influence of process parameters on microstructure development*

The experimental results demonstrate that the initial near-SX substrate texture cannot be fully maintained under any of the investigated processing conditions, as evidenced by the initial decrease in the M-index observed for all samples (Fig. 8). Nevertheless, the extent of texture degradation strongly depends on the processing parameters. In general, higher laser powers and lower scan speeds, corresponding to, resulted in stronger texture retention, lower HAGB densities, larger ODF peak intensities, and a reduced tendency for the $\{001\}_z\langle 110\rangle_x$ to $\{001\}_z\langle 100\rangle_x$ texture transition.

These observations are consistent with the thermal characteristics previously reported for flat-top laser processing of HX [34]. Higher energy densities produce wider and deeper melt pools and increase the local temperature within the deposited material. As a consequence, the temperature gradient G, solidification rate R, and cooling rate $G \times R$ decrease. Reduced solidification kinetics promote coarser dendritic structures and larger grains, while simultaneously stabilizing the solidification front and reducing the probability of heterogeneous nucleation. Experimentally, this behavior is reflected by the decrease in HAGB density and the increase in texture strength observed at higher laser powers.

The influence of scan speed is more complex because it simultaneously modifies both the local energy input and the thermal history of the build. Increasing the scan speed reduces the energy delivered per unit length, resulting in smaller melt pools and generally weaker texture retention. However, higher scan speeds also reduce the time interval between successive layers, which may enhance heat accumulation within the sample. The resulting decrease in thermal gradients can partially compensate for the reduction in energy density, explaining why scan speed does not always produce monotonic changes in texture strength.

The CA simulations reproduce the overall dependence of texture evolution on process parameters. For a given nucleation density, higher energy density conditions generate larger melt pools and increased remelting depths, allowing grains to experience repeated melting-solidification cycles. These repeated cycles promote the selection and persistence of favorably oriented grains over larger distances. In contrast, lower energy density conditions produce smaller melt pools, higher thermal gradients, and faster solidification rates. Under these conditions, newly nucleated grains contribute more significantly to the final microstructure, leading to higher HAGB densities, weaker textures, and a faster evolution away from the initial substrate orientation.

Although the simulations correctly reproduce the overall trends, they generally predict a stronger dependence of texture evolution on processing parameters than observed experimentally. In particular, the transition towards the $001z\langle 100\rangle x$ texture is predicted to occur more rapidly than measured experimentally, suggesting that additional mechanisms not included in the present model contribute to the stabilization of the inherited texture.

4.2. *Nucleation activity and texture evolution*

The CA simulations confirm that nucleation activity is one of the dominant parameters controlling microstructure and texture evolution during the build process. Among the investigated conditions, nucleation densities in the range $N_0 = 10\text{–}20 \times 10^{12}$ m^{-3} provided the closest agreement with the experimentally measured M-index evolution. These values are comparable to those reported in previous CA studies of additive manufacturing [28,30]. It should be noted that the nucleation model employed in the present work is probabilistic. The nucleation density, mean nucleation undercooling, and standard deviation collectively determine the effective nucleation activity within the melt pool. Consequently, the selected nucleation density should not be interpreted

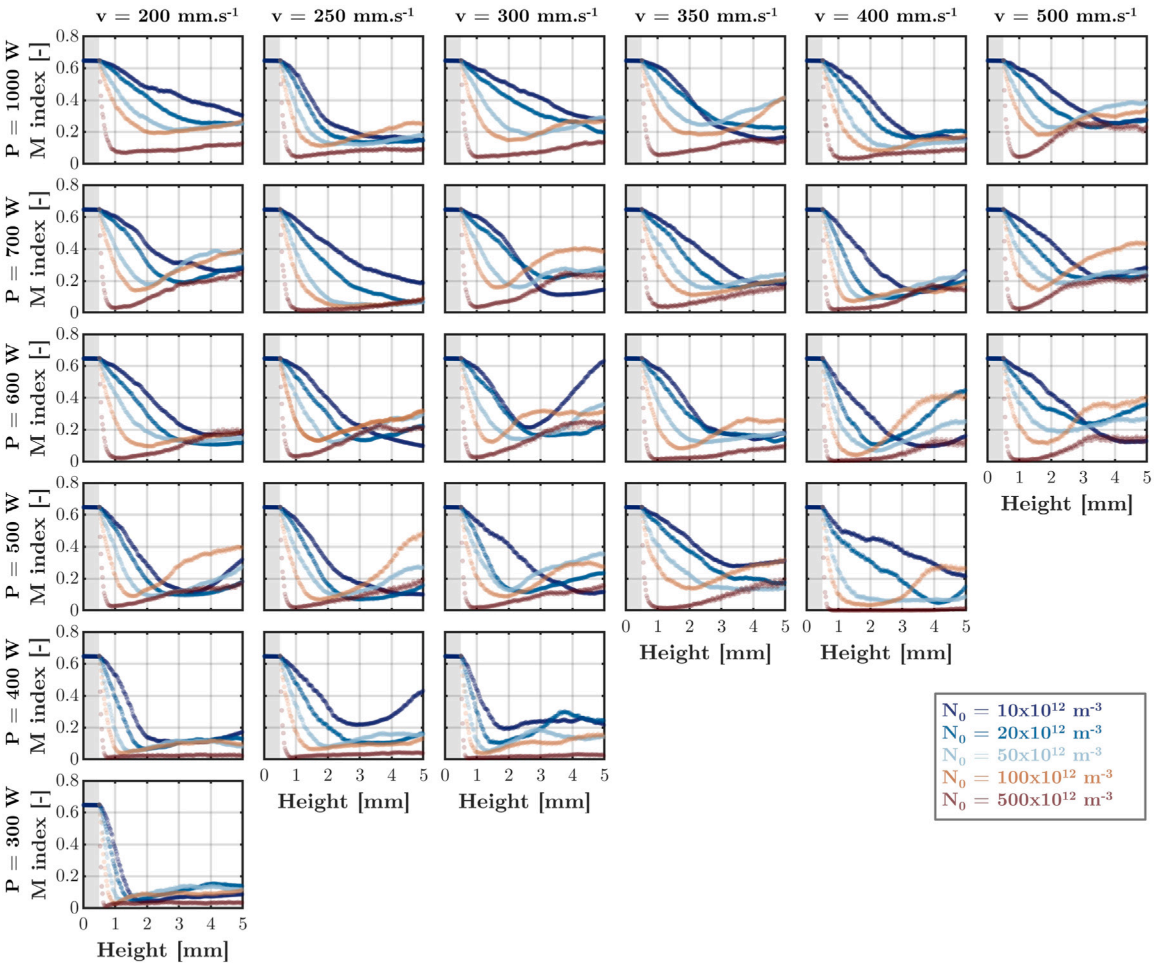

Fig. 12. Variation of the M-index along the build height predicted for the different build conditions and nucleation densities.

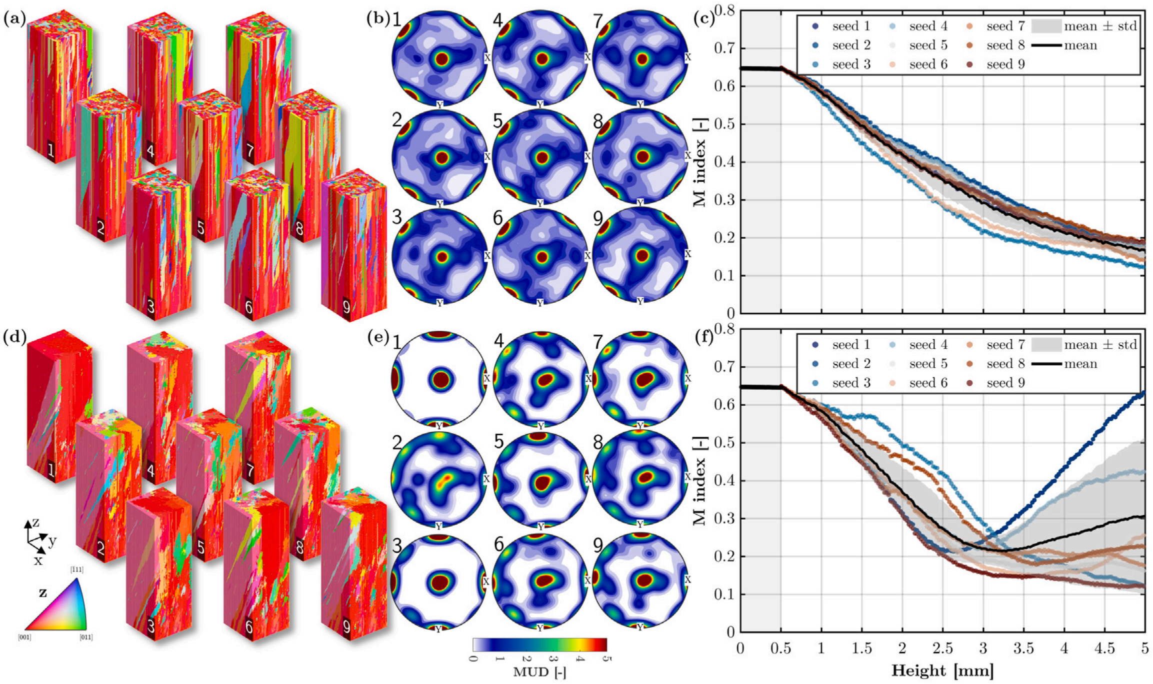

Fig. 13. (a,d) Numerical microstructures predicted by CA for nine different random number generation seed, (b,e) corresponding (100) pole figures and (c,f) variation of the M-index along the build height for (a–c) P = 700 W, v = 250 mm s^{-1} and (d–f) P = 600 W, v = 300 mm s^{-1}. The solid black line represents the mean M-index calculated from the nine simulations, while the shaded region indicates one standard deviation.

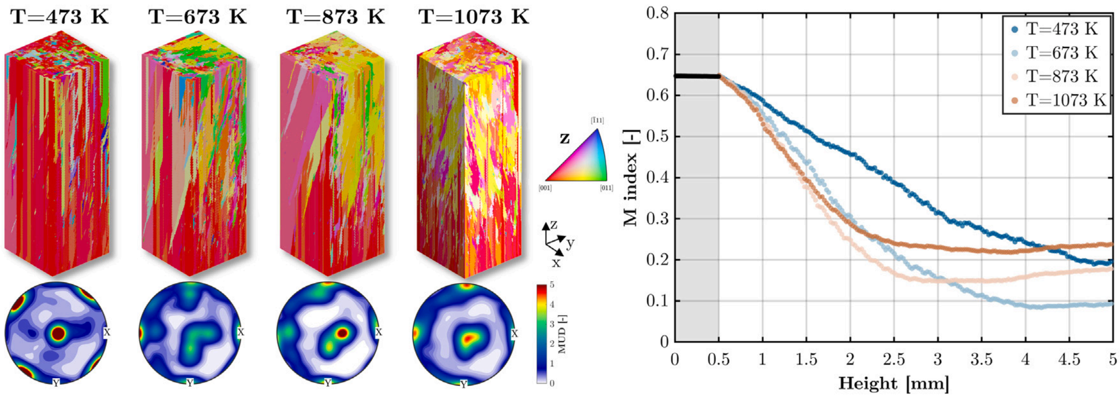

Fig. 14. (a) Numerical microstructures predicted by CA with a laser power P = 700 W, a scan speed v = 250 mm s^{-1} and for four different substrate temperatures and corresponding (100) pole figures. (b) Variation of the M-index along the build height for four microstructures.

as a unique physical quantity, but rather as a representative parameter controlling the frequency of successful nucleation events during solidification. A notable observation is that neither the experiments nor the simulations reached a clear steady-state texture after 4.5 mm of build height. Instead, the M-index continued to evolve throughout the build, indicating that the balance between texture degradation and texture recovery remained active. This behavior suggests that the microstructure remains strongly influenced by the inherited substrate texture over a considerable build height.

Increasing nucleation activity systematically modifies both the microstructure and texture descriptors. Higher nucleation densities produce finer grains, increase the HAGB density, decrease the ODF peak intensity, and accelerate the reduction of the M-index. In addition, increasing nucleation activity promotes a progressive transition from the inherited$\{001\}_z\langle 110\rangle_x$ texture towards a $\{001\}_z\langle 100\rangle_x$ texture. This trend is reflected by increasing values of $f_{\langle 100\rangle}$ and R_{100} together with decreasing values of $f_{\langle 110\rangle}$. The emergence of a $001z\langle 100\rangle x$ Cube texture is commonly reported in fcc alloys fabricated using Gaussian laser systems and zig-zag scanning strategies [8,9,42]. In contrast, the experimental results obtained using the flat-top laser indicate a greater stability of the $001z\langle 110\rangle x$ texture, consistent with previous observations in pure Ni processed under similar conditions [15,16]. While the simulations successfully reproduce the existence of both texture states, they generally predict a faster transition towards $001z\langle 100\rangle x$ than observed experimentally. This discrepancy indicates that the present framework may not fully capture the balance between nucleation and epitaxial growth during solidification. In particular, uncertainties associated with the nucleation model, grain selection mechanisms, and the thermal fields used to drive the CA simulations may influence the predicted texture evolution. The potential impact of these assumptions and their associated limitations are discussed in the following section.

4.3. Limitations of the approach

4.3.1. Thermal model uncertainties

The reliability of the CA predictions is inherently dependent on the accuracy of the thermal model, since the melt-pool geometry and local thermal gradients directly determine grain growth directions and the competition between epitaxial growth and nucleation. As shown in Fig. 6, the thermal model reproduces most melt-pool dimensions with good agreement but exhibits larger discrepancies at the lowest and highest energy densities. It should be noted that the thermal model was calibrated using melt-pool width and depth measurements obtained from two experimental single-track scans for each processing condition, and a single set of heat-source parameters was used across the entire process window.

At low energy densities, the experimental melt-pool dimensions exhibited increased variability, contributing to the observed discrepancies between simulations and experiments. For example, the experimentally measured melt-pool widths and depths did not always vary monotonically with substrate temperature, whereas the thermal model predicted a systematic increase in melt-pool dimensions with increasing preheating temperature. This behavior may be related to localized variations in the flat-top laser beam profile at low power, where the power distribution may deviate from the ideal uniform profile [14].

At high energy densities, additional discrepancies were observed in the melt-pool shape. While the simulated melt pools retained a relatively smooth semi-circular geometry characteristic of conduction mode, the experimental melt pools exhibited flatter bottoms, steeper side walls, and, in some cases, inflection points along the melt-pool boundary. These features cannot be reproduced by the present model because it only solves the heat equation and neglects melt flow, free-surface deformation, volume shrinkage, evaporation, and recoil pressure effects. Such phenomena are known to influence melt-pool morphology and solidification conditions [44].

Consequently, some uncertainty is expected in the corresponding CA predictions. In particular, inaccuracies in melt-pool dimensions and shape may alter the local growth conditions, influencing grain selection, texture development, and the probability of nucleation events. Nevertheless, the overall trends observed in the simulations are expected to remain qualitatively robust because the predicted melt-pool dimensions remain close to the experimental values over most of the investigated process window. Furthermore, the use of a single calibrated parameter set over a broad range of processing conditions provides confidence that the model captures the dominant thermal trends rather than being optimized for a limited number of cases. Future work could improve the representation of melt-pool geometry through coupling with fluid-flow simulations or by employing more sophisticated heat-source formulations capable of reproducing the experimentally observed melt-pool shapes [45].

4.3.2. Thermal history simplifications

In addition, the temperature fields from single-track simulations were used to drive the solidification process across the build height in the CA model. While this approach captures the primary effects of process parameters on grain evolution, it does not account for the progressive temperature accumulation within the sample as additional layers are built. As the build proceeds, this heat accumulation leads to a gradual reduction in thermal gradients, cooling rates, and solidification rates, while simultaneously increasing the melt pool width and depth (Fig. 6). The omission of these evolving thermal conditions represents a limitation of the current model, as they can significantly influence grain selection dynamics. From a microstructural perspective, reduced thermal gradients and slower solidification rates are expected to modify the balance between nucleation and epitaxial growth. In particular, lower thermal gradients decrease the driving force for heterogeneous nucleation and promote the persistence of columnar growth [46]. However, at early stages of the build, especially for low initial substrate temperatures, relatively high thermal gradients can still promote nucleation events, contributing to the initial degradation of the inherited texture. As heat progressively accumulates, the solidification conditions evolve toward a regime more favorable to epitaxial growth, which can lead to a recovery and subsequent strengthening of the crystallographic texture at larger build heights. The additional simulations performed at higher substrate temperatures support this interpretation (Fig. 14). Increasing the initial substrate temperature effectively mimics an advanced stage of thermal accumulation, leading to reduced thermal gradients from the beginning of the build. As a result, a more pronounced initial texture drop may occur due to altered early-stage solidification conditions, but this is followed by a stronger recovery of the texture as stable melt pools and repeated remelting cycles enhance epitaxial growth. These observations highlight that the balance between nucleation and epitaxial growth is not constant but evolves dynamically with the thermal history of the sample. The extent of heat accumulation depends not only on the process parameters but also on the geometry of the build [47]. Consequently, it is reasonable to assume that nucleation density should not be treated as constant throughout the build height, but rather as a variable parameter that evolves with the local thermal conditions. This effect may also contribute to discrepancies in texture predictions, particularly in the xy-plane. As thermal gradients become more isotropic due to prolonged heat accumulation, in-plane grain orientations may progressively reorient by approximately 45° relative to the scan and hatch directions. The present CA model does not explicitly account for this thermal history evolution, which likely contributes to the observed differences between experimental and simulated texture evolution. Future modeling efforts should therefore incorporate layer-by-layer thermal history effects to improve the accuracy of microstructure predictions.

4.3.3. Sources of uncertainty in microstructure prediction

In the present study, the uncertainty associated with the stochastic nature of heterogeneous nucleation location was investigated by varying the random number generator seed under two different process conditions (Fig. 12). The results reveal that the variability in the predicted microstructure introduced by changing the random seed is not uniform across different processing conditions. While some conditions produce robust and repeatable grain structures (Fig. 12(a–c)), others exhibit high sensitivity to stochastic effects, leading to significant deviations in microstructure evolution (Fig. 12(d–f)). The random number seed affects two key aspects of nucleation: (1) the spatial location of newly nucleated grains and (2) their crystallographic orientation. In the present model, the crystal orientation of a new grain is sampled from a list of 10,000 randomly generated orientations derived from a uniform ODF. This approach ensures statistical randomness in grain orientation selection while preserving a uniform texture distribution at the nucleation stage. A particularly interesting observation is that in certain process conditions, variations in the random seed do not significantly alter the final grain structure. Conversely, for other conditions, small perturbations in the nucleation seed result in drastic changes in final texture and grain morphology. This behavior is typically observed in cases where nucleation events strongly influence microstructure formation, such as at lower linear energy densities, where epitaxial growth is weaker, and nucleation-driven grain formation dominates. Previous study showed that this effect was more pronounced the coarser the substrate grains [32]. The present study is in agreement with this observation but also suggest that it may also depends on the process conditions. The observed variability emphasizes the need for probabilistic modeling approaches when predicting microstructures in AM. Instead of relying on a single deterministic simulation, ensemble modeling, where multiple simulations with different seeds are averaged, could provide a more accurate representation of the expected microstructure distribution. Additionally, incorporating experimentally measured nucleation site distributions rather than purely random assignments could further enhance model reliability.

4.3.4. Domain and cell size effects

The abnormal growth of a single dominant grain observed in some simulations should be interpreted with caution. While such behavior is physically plausible in highly textured systems where a favorably oriented grain outcompletes neighboring grains during repeated epitaxial growth, the frequency and extent of this phenomenon may be influenced by numerical assumptions adopted in the present framework. In particular, the finite lateral dimensions of the simulation domain reduce the number of competing grains available during growth, potentially increasing the probability that a single grain eventually occupies a large fraction of the domain. This limitation is particularly relevant in the present study because the flat-top laser diameter (~700 μm) is substantially larger than the Gaussian beam diameters typically considered in previous CA studies of additive manufacturing, which are often on the order of 100 μm. To capture the melt-pool geometry and texture evolution under these conditions, a computational domain of $1500 \times 1500 \times 4500$ μm^3 was employed with a cell size of 5 μm. Although this domain spans more than twice the laser spot diameter and contains several million CA cells, it remains small relative to the dimensions of the melt pool, especially at high energy density. The selected cell size of 5 μm is also consistent with the spatial resolutions commonly employed in CA simulations of additive manufacturing [21,22,30,35,48,49]. Although a finer spatial discretization would allow a more detailed description of newly nucleated grains, it would also substantially increase the computational cost due to the large melt-pool dimensions associated with the flat-top laser. In addition, the nucleation density parameter is inherently linked to the discretization of the computational domain, as the number of potential nucleation sites depends on the cell volume. Consequently, a direct comparison of simulations performed with different cell sizes would require a corresponding recalibration of the nucleation parameters.

Furthermore, the repeated application of a simplified thermal history may promote the persistence of favorable growth conditions over extended build heights. Therefore, although the emergence of dominant grains is consistent with the grain-selection mechanisms expected during directional solidification, the quantitative extent and frequency of the observed abnormal grain growth should not be interpreted as fully predictive results.

4.3.5. Additional physical effects

The present CA model also treats the substrate primarily as a crystallographic template and does not explicitly account for chemical interactions between the pure Ni substrate and the deposited HX alloy. In practice, partial remelting of the substrate during the first deposited layers creates a chemically mixed region at the interface, as evidenced by the EDS measurements reported in our previous experimental study [34]. The resulting dilution and compositional gradients may locally modify thermophysical properties, solidification conditions, and constitutional undercooling. In particular, segregation of alloying elements such as Cr, Mo, and Fe near the interface may influence nucleation behavior and the stability of epitaxial growth. Previous observations also showed that stray grain formation frequently initiates near the substrate-deposit interface, where both crystallographic and compositional effects interact. Since these phenomena are not explicitly considered in the present framework, the model may not fully capture the microstructural evolution occurring during the first deposited layers.

Another limitation of the present framework is that the development of residual stresses during additive manufacturing was not considered. Residual stresses arise from the large thermal gradients and repeated thermal cycling experienced during the build process and may influence distortion, defect formation, cracking susceptibility, and the final mechanical properties of the material. In addition, residual stresses can affect the local driving forces for recovery, recrystallization, and grain boundary migration, potentially influencing microstructure evolution during processing. While solidification conditions and nucleation behavior are expected to be the dominant factors controlling the texture evolution investigated in the present work, the interaction between residual stress development and microstructure evolution warrants further investigation. Future studies could benefit from coupling the thermal and microstructure models with mechanical simulations to account for stress evolution during the build process [50].

5. Conclusions

The present study focused on the texture development simulation in AM HX samples produced on top of a near-SX Ni substrate using a flat-top laser with different process parameters through a combined experimental–numerical approach using the CA method. The CA simulations were driven by temperature field extracted from thermal simulations solely based on the heat equation and calibrated against single track experiments. It was confirmed that flat-top laser can be modeled as a circular surface beam with a uniform distribution resulting in melt pools with low depth-to-width ratio. The experimental results demonstrated that the initial near-SX substrate texture could not be fully maintained, as indicated by a sharp drop in the M-index for all process conditions. CA simulations successfully reproduced the initial texture drop and showed that higher energy densities favor epitaxial growth, reducing the frequency of new grain nucleation. While the simulations correctly reproduced the $\{001\}_z$ texture, it also predicted a transition from the $\langle 110\rangle_x$ texture towards the $\langle 100\rangle_x$ orientation which was not always observed experimentally. This suggested that the present modeling approach using thermal field from single track simulation may be insufficient as it neglects the heat accumulation within the sample. Finally, the stochastic aspect introduced by the randomness of the grain nucleation process and the random number generator seed was found to have different effect depending on the simulation condition and highlighted the need for probabilistic modeling approaches.

Declaration of competing interest

The authors declare that they have no known competing financial interests or personal relationships that could have appeared to influence the work reported in this paper.

Acknowledgments

This work was supported by “Innovative Science and Technology Initiative for Security, Grant Number JPJ004596 implemented by the Acquisition, Technology, and Logistics Agency (ATLA), Japan” and also was financially supported by “The Amada Foundation (Grant Number AF-2022201-A3) . This work was partly supported by K Program Grant Number JPMJKP25R1 (Funding agency: JST).

Appendix A. Supplementary data

Supplementary material related to this article can be found online at https://doi.org/10.1016/j.jmrt.2026.06.251.

Data availability

The raw/processed data are available from the corresponding author upon reasonable request.

References

[1] Frazier WE. Metal additive manufacturing: A review. J Mater Eng Perform 2014;23:1917–28.

[2] DebRoy T, Wei HL, Zuback JS, Mukherjee T, Elmer JW, Milewski JO, Beese AM, Wilson-Heid A, De A, Zhang W. Additive manufacturing of metallic components – Process, structure and properties. Prog Mater Sci 2018;92:112–224.

[3] Liu G, Zhang X, Chen X, He Y, Cheng L, Huo M, Yin J, Hao F, Chen S, Wang P, Yi S, Wan L, Mao Z, Chen Z, Wang X, Cao Z, Lu J. Additive manufacturing of structural materials. 2021.

[4] Vafadar A, Guzzomi F, Rassau A, Hayward K. Advances in metal additive manufacturing: A review of common processes, industrial applications, and current challenges. Appl Sci 2021;11:1–33.

[5] Helmer H, Bauereiß A, Singer RF, Körner C. Grain structure evolution in Inconel 718 during selective electron beam melting. Mater Sci Eng: A 2016;668:180–7.

[6] Kirka MM, Lee Y, Greeley DA, Okello A, Goin MJ, Pearce MT, Dehoff RR. Strategy for texture management in metals additive manufacturing. JOM 2017;69:523–31.

[7] Suwas S, Vikram RJ. Texture evolution in metallic materials during additive manufacturing: A review. Trans Indian Natl Acad Eng 2021;6:991–1003.

[8] Ishimoto T, Hagihara K, Hisamoto K, Sun SH, Nakano T. Crystallographic texture control of beta-type Ti–15Mo–5Zr–3Al alloy by selective laser melting for the development of novel implants with a biocompatible low Young’s modulus. Scr Mater 2017;132:34–8.

[9] Ishimoto T, Wu S, Ito Y, Sun SH, Amano H, Nakano T. Crystallographic orientation control of 316l austenitic stainless steel via selective laser melting. ISIJ Int 2020;60:1758–64.

[10] Hagihara K, Nakano T. Control of anisotropic crystallographic texture in powder bed fusion additive manufacturing of metals and ceramics—A review. 2021.

[11] Ishimoto T, Morita N, Ozasa R, Matsugaki A, Gokcekaya O, Higashino S, Tane M, Mayama T, Cho K, Yasuda HY, Okugawa M, Koizumi Y, Yoshiya M, Egusa D, Sasaki T, Abe E, Kimizuka H, Ikeo N, Nakano T. Superimpositional design of crystallographic textures and macroscopic shapes via metal additive manufacturing—Game-change in component design. Acta Mater 2025;286.

[12] Kumar D, Shankar G, Prashanth KG, Suwas S. Control of texture and microstructure in additive manufacturing of stainless steel 316 L. J Alloys Compd 2024;976.

[13] Tenbrock C, Fischer FG, Wissenbach K, Schleifenbaum JH, Wagenblast P, Meiners W, Wagner J. Influence of keyhole and conduction mode melting for top-hat shaped beam profiles in laser powder bed fusion. J Mater Process Technol 2020;278.

[14] Pilz S, Gustmann T, Günther F, Zimmermann M, Kühn U, Gebert A. Controlling the Young’s modulus of a β -type Ti–Nb alloy via strong texturing by LPBF. Mater Des 2022;216.

[15] Jodi DE, Kitashima T, Koizumi Y, Nakano T, Watanabe M. Manufacturing single crystals of pure nickel via selective laser melting with a flat-top laser beam. Addit Manuf Lett 2022;3.

[16] Jodi DE, Kitashima T, Watanabe M. Effect of scan strategy on the formation of a pure nickel single-crystal structure using a flat-top laser beam via laser powder bed fusion. Sci Technol Adv Mater 2023;24.

[17] Gandin C-A, Desbiolles J-L, Rappaz M, Thé P, Voz T. A three-dimensional cellular automaton-finite element model for the prediction of solidification grain structures. Met Mater Trans A 1999;3153–65.

[18] Zinovieva O, Zinoviev A, Ploshikhin V, Romanova V, Balokhonov R. A solution to the problem of the mesh anisotropy in cellular automata simulations of grain growth. Comput Mater Sci 2015;108:168–76.

[19] Zhang J, Liou F, Seufzer W, Taminger K. A coupled finite element cellular automaton model to predict thermal history and grain morphology of Ti–6Al–4V during direct metal deposition (DMD). Addit Manuf 2016;11:32–9.

[20] Chen S, Guillemot G, Gandin CA. Three-dimensional cellular automaton-finite element modeling of solidification grain structures for arc-welding processes. Acta Mater 2016;115:448–67.

[21] Zinoviev A, Zinovieva O, Ploshikhin V, Romanova V, Balokhonov R. Evolution of grain structure during laser additive manufacturing. Simulation by a cellular automata method. Mater Des 2016;106:321–9.

[22] Zinovieva O, Zinoviev A, Ploshikhin V. Three-dimensional modeling of the microstructure evolution during metal additive manufacturing. Comput Mater Sci 2018;141:207–20.

[23] Yang J, Yu H, Yang H, Li F, Wang Z, Zeng X. Prediction of microstructure in selective laser melted Ti–6Al–4V alloy by cellular automaton. J Alloys Compd 2018;748:281–90.

[24] Lian Y, Lin S, Yan W, Liu WK, Wagner GJ. A parallelized three-dimensional cellular automaton model for grain growth during additive manufacturing. Comput Mech 2018;61:543–58.

[25] Robichaud J, Vincent T, Schultheis B, Chaudhary A. Integrated computational materials engineering to predict melt-pool dimensions and 3D grain structures for selective laser melting of Inconel 625. Integr Mater Manuf Innov 2019;8:305–17.

[26] Lian Y, Gan Z, Yu C, Kats D, Liu WK, Wagner GJ. A cellular automaton finite volume method for microstructure evolution during additive manufacturing. Mater Des 2019;169.

[27] Xiong F, Huang C, Kafka OL, Lian Y, Yan W, Chen M, Fang D. Grain growth prediction in selective electron beam melting of Ti–6Al–4V with a cellular automaton method. Mater Des 2021;199.

[28] Rolchigo M, Reeve ST, Stump B, Knapp GL, Coleman J, Plotkowski A, Belak J. ExaCA: A performance portable exascale cellular automata application for alloy solidification modeling. Comput Mater Sci 2022;214.

[29] Sabau AS, Yuan L, Fattebert JL, Turner JA. An OpenMP GPU-offload implementation of a non-equilibrium solidification cellular automata model for additive manufacturing. Comput Phys Comm 2023;284.

[30] Liang X, Zhu J, Popovich V, Hermans M, Richardson I, Bos C. A multi-level capture algorithm for accelerating cellular automata predictions of grain structure and texture in additive manufacturing. Addit Manuf 2025;98.

[31] Rolchigo M, Stump B, Belak J, Plotkowski A. Sparse thermal data for cellular automata modeling of grain structure in additive manufacturing. Modelling Simul Mater Sci Eng 2020;28.

[32] Rolchigo M, Carson R, Belak J. Understanding uncertainty in microstructure evolution and constitutive properties in additive process modeling. Metals 2022;12.

[33] Knapp GL, Coleman J, Rolchigo M, Stoyanov M, Plotkowski A. Calibrating uncertain parameters in melt pool simulations of additive manufacturing. Comput Mater Sci 2023;218.

[34] Daram P, Briffod F, Kitashima T, Kusano M, Watanabe M. Effects of substrate preheating and processing parameters on the crystallographic texture of Hastelloy X on SX-like Ni fabricated by L-PBF process with flat-top laser beam. J Mater Res Technol 2026;41:1974–85.

[35] Briffod F, Daram P, Kusano M, Watanabe M. An integrated computational materials engineering framework for process–structure–property mapping in laser powder bed fusion. Mater Des 2025;260.

[36] Coleman J, Knapp GL, Stump B, Rolchigo M, Kincaid K, Plotkowski A. A dynamic volumetric heat source model for laser additive manufacturing. Addit Manuf 2024;95.

[37] Mills KC. Recommended Values of Thermophysical Properties for Selected Commercial Alloys. Woodhead; 2002, p. 244.

[38] Gandin C-A, Rappaz M. A 3D cellular automaton algorithm for the prediction of dendritic grain growth. 1997, p. 2187–95.

[39] Kurz W, Giovanola B, Trivedi R. Theory of I rostructural development during rapid solidification. Acta Metall 1986;34:823.

[40] Bachmann F, Hielscher R, Schaeben H. Texture analysis with MTEX- free and open source software toolbox. In: Solid state phenomena. 2010;vol. 160:63–8.

[41] Skemer P, Katayama I, Jiang Z, Karato SI. The misorientation index: Development of a new method for calculating the strength of lattice-preferred orientation. Tectonophysics 2005;411:157–67.

[42] Ishimoto T, Hagihara K, Hisamoto K, Nakano T. Stability of crystallographic texture in laser powder bed fusion: Understanding the competition of crystal growth using a single crystalline seed. Addit Manuf 2021;43.

[43] Tang J, Kumar S, Lorenzis LD, Hosseini E. Neural cellular automata for solidification microstructure modelling. Comput Methods Appl Mech Engrg 2023;414.

[44] Pantawane MV, Ho YH, Joshi SS, Dahotre NB. Computational assessment of thermokinetics and associated microstructural evolution in laser powder bed fusion manufacturing of Ti6Al4V alloy. Sci Rep 2020;10.

[45] Kusano M, Watanabe M. Heat source model development for thermal analysis of laser powder bed fusion using Bayesian optimization and machine learning. Integr Mater Manuf Innov 2024;13:288–304.

[46] Zhao W, Sun Y, Che P, Ning Z, Fan H, Yang H, Sun J, Liaw PK, Ngan AH, Huang Y. The columnar to equiaxed transition of CoCrNi medium-entropy alloy fabricated by laser directed energy deposition. Mater Des 2024;237.

[47] Kusano M, Watanabe M. Controlling heat accumulation through changing time per layer in laser powder bed fusion of nickel-based superalloy. J Manuf Process 2024;131:187–98.

[48] Zinovieva O, Zinoviev A, Romanova V, Balokhonov R. Three-dimensional analysis of grain structure and texture of additively manufactured 316L austenitic stainless steel. Addit Manuf 2020;36.

[49] Teferra K, Rowenhorst DJ. Optimizing the cellular automata finite element model for additive manufacturing to simulate large microstructures. Acta Mater 2021;213.

[50] Abdelaal AF, Chakrobarty A, Sakib MN, Arka AM, Sabuz EH. Porosity, residual stress, wear properties and impact toughness of additively manufactured low-alloy steel: A review. Next Mater 2025;9.